.

THE SUN [1]

Markus J. Aschwanden
Lockheed Martin ATC, Solar & Astrophysics Laboratory

Glossary

Alfvén waves: A wave propagating in a magnetized plasma in which the magnetic field oscillates transverse to the propagation direction. The propagation speed is given by the Alfvén speed $v_A = B/\sqrt{4\pi\rho}$, where B is the magnetic field strength and ρ the mass density, named after Hannes Alfvén.

Bremsstrahlung: Electromagnetic radiation that is emitted when an energetic electron is deflected by an ion. It is also called *free-free emission*, because both the electron and ion are free in an ionized plasma. The term is borrowed from German and means *"braking radiation"*, because the deflected electron loses energy (by the emitted photon) and is slowed down.

Chromosphere: Lower atmosphere of the Sun, above the photosphere and beneath the transition region, with a vertical height extent of about 2000 km and a temperature range of 6000-20,000 K.

Corona: Upper atmosphere of the Sun, extending above the transition region out into the heliosphere, with a dominant temperature of 1-2 million K in the lowest 100,000 km.

Coronal Mass Ejection (CME): Magnetic instabilities in the solar corona lead to eruption of filaments, prominences, and magnetic flux ropes, which propagate as ejected mass out into the heliosphere, often accompanied by a flare phenomenon.

Filaments: Near-horizontal magnetic field lines suspended above magnetic inversion lines that are filled with cool and dense chromospheric mass, seen on the solar disk.

Flares: A magnetic instability in the solar corona that releases impulsively large energies that go into heating of coronal and chromospheric plasma, as well as into acceleration of high-energy particles. A flare is usually accompanied by impulsive emission in gamma-rays, hard X-rays, soft X-rays, EUV, and radio emission.

Heliosphere: The entire space of the solar system that is permeated by the solar wind, bound by the heliopause where the solar wind balances that of the interstellar medium.

Magnetic Reconnection: A magnetic instability can be triggered in the solar corona, where the topology and connectivity of magnetic field line changes, believed to be the primary cause of flares and CMEs.

---

[1]Chapter *The Sun* by Markus J. Aschwanden, for the *Encyclopedia of the Solar System*, 2^{nd} edition, 2005, (eds. Lucy-Ann McFadden, Paul Weissman, & Torrence Johnson), Academy Press, Elsevier Science, Amsterdam, The Netherlands.

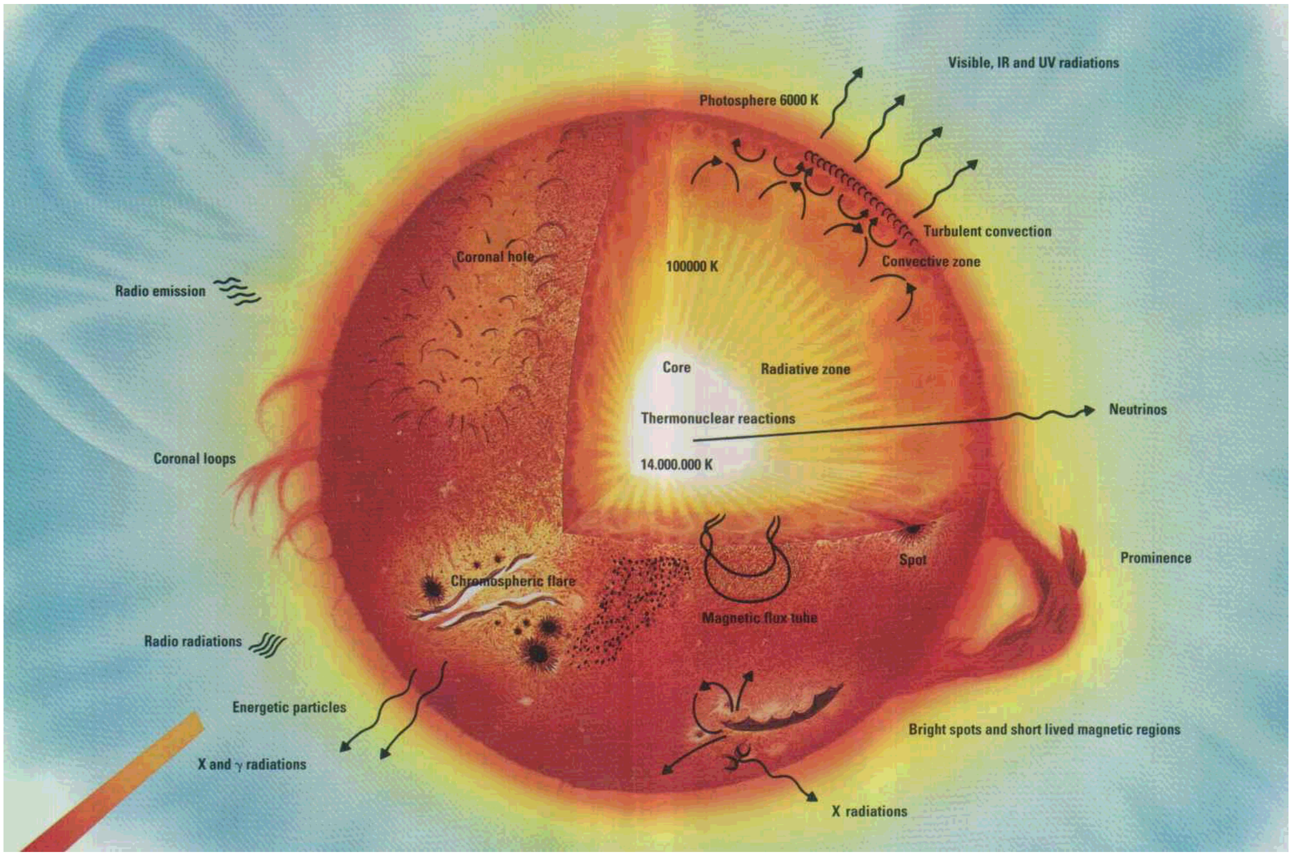

Figure 1: A cutaway view of the Sun, showing the three internal (thermonuclear, radiative, and convective) zones, the solar surface (photosphere), the lower (chromosphere) and upper atmosphere (corona), and a number of phenomena associated with the solar activity cycle (filaments, prominences, flares), (courtesy of Cavin J. Hamilton and NASA/ESA).

Photosphere: A thin 300-km thick layer above the solar surface from where most of the optical emission (white light) is irradiated, with a temperature of ≈6000 K.

Prominences: Cool and dense mass structures suspended above the chromosphere, observed above the solar limb, which are called filaments when seen on the solar disk.

Transition Region: It demarcates the vertical zone where the temperature climbs from 20,000 K above the cool chromosphere to 1 million K in the hot corona.

1 Introduction

The Sun is the central body and energy source of our solar system. The Sun is our nearest star, but otherwise represents a fairly typical star in our galaxy, classified as *G2-V* spectral type, with a radius of $r_\odot \approx 700,000$ km, a mass of $m_\odot \approx 2 \times 10^{33}$ g, a luminosity of $L_\odot \approx 3.8 \times 10^{26}$ W, and an age of $t_\odot \approx 4.6 \times 10^9$ years (Table 1). The distance of the Sun to our Earth is called an *Astronomical Unit (AU)* and amounts to $\approx 150 \times 10^6$ km. The Sun lies in a spiral arm of our galaxy, the *Milky Way*, at a distance of 8.5 kiloparsecs from the galactic center. While our galaxy contains $\approx 10^{12}$ individual stars, many of the single stars are likely to be populated with similar solar systems, according to the rapidly increasing detection of *extra-solar planets* over the last years, while binary star systems are very unlikely to harbor planets because of their unstable, gravitationally disturbed orbits. The Sun is

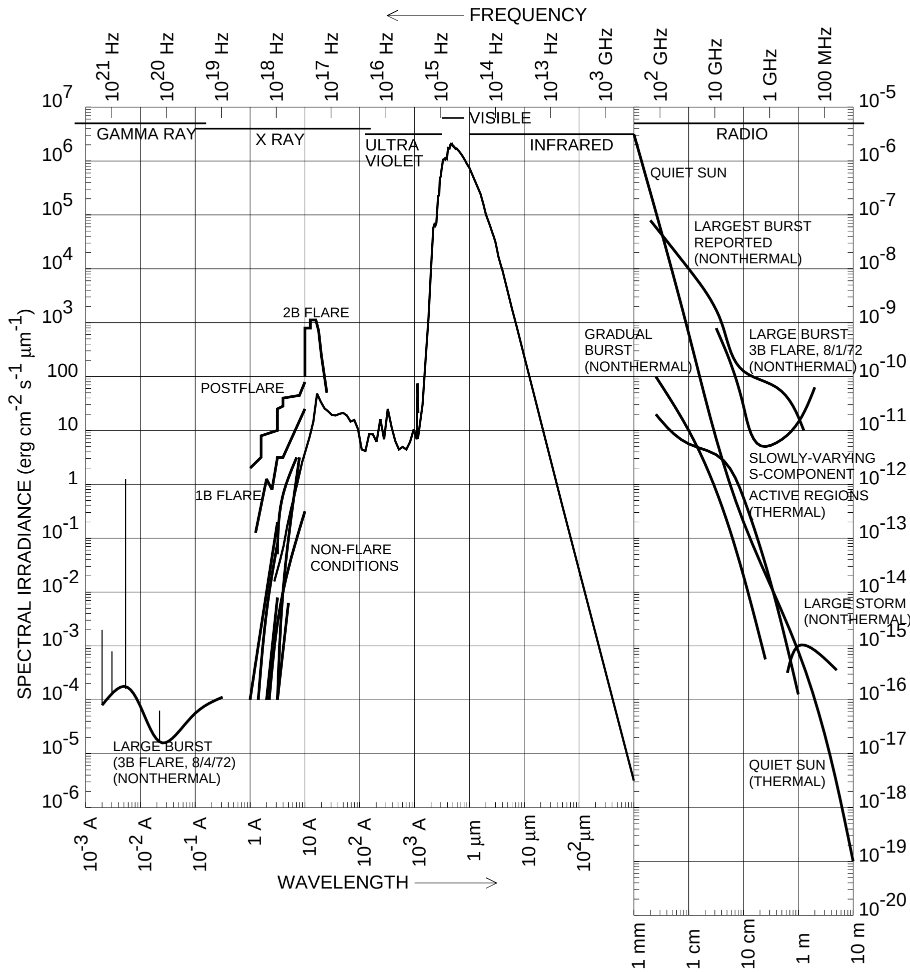

Figure 2: The solar irradiance spectrum from gamma-rays to radio waves. The spectrum is shifted by 12 orders of magnitude in the vertical axis at $\lambda = 1$ mm to accommodate for the large dynamic range in spectral irradiance (courtesy of H. Malitson and NASA/NSSDC).

for us humans of particular significance, first because it provides us with the source of all life, and second because it furnishes us with the closest laboratory for astrophysical plasma physics, magneto-hydrodynamics (MHD), atomic physics, and particle physics. The Sun still represents the only star from which we can obtain spatial images, in many wavelengths.

The basic structure of the Sun is sketched in Fig. 1. The Sun and the solar system were formed together from an interstellar cloud of molecular hydrogen, some 5 billion years ago. After gravitational contraction and subsequent collapse, the central object became the Sun, with a central temperature hot enough to ignite thermonuclear reactions, the ultimate source of energy for the entire solar system. The chemical composition of the Sun consists of 92.1% hydrogen and 7.8% helium by number (or 27.4% He by mass), and 0.1% of heavier elements (or 1.9% by mass, mostly C, N, O, Ne, Mg, Si, S, Fe). The *central core*, where hydrogen burns into helium, has a temperature of ≈15 million K (Fig. 1). The solar interior further consists of a *radiative zone*, where energy is transported mainly by radiative diffusion, a process where photons with hard X-ray (keV) energies get scattered, absorbed, and re-emitted. The outer third of the solar interior is called the *convective zone*, where energy is transported mostly by convection. At the solar surface, photons leave the Sun in optical wavelengths, with an energy that is about a factor of 10^5 lower than the original hard X-ray photons generated in the nuclear core, after a random walk of $\approx 10^5 - 10^6$ years.

Physical parameter	Numerical value
Solar radius	$R_{\odot} = 695,500$ km
Solar mass	$m_{\odot} = 1.989 \times 10^{33}$ g
Mean density	$\rho_{\odot} = 1.409$ g cm^{-3}
Gravity at solar surface	$g_{\odot} = 274.0$ m s^{-2}
Escape velocity at solar surface	$v = 617.7$ km s^{-1}
Synodic rotation period	$P = 27.3$ days (equator)
Sidereal rotation period	$P = 25.4$ days (equator)
	$P = 35.0$ days (at latitude $\pm 70^0$)
Mean distance from Earth	1 AU = 149,597,870 km
Solar luminosity	$L_{\odot} = 3.844 \times 10^{26}$ W (or 10^{33} ergs s^{-1})
Solar age	$t_{\odot} = 4.57 \times 10^9$ years
Temperature at Sun center	$T_c = 15.7 \times 10^6$ K
Temperature at solar surface	$T_{ph} = 6400$ K

Table 1: Basic physical properties of the Sun (from Allen's Astrophysical Quantities).

The irradiance spectrum of the Sun is shown in Fig.2, covering all wavelengths from gamma-rays, hard X-rays, soft X-rays, extreme ultraviolet (EUV), ultraviolet, white light, infrared, to radio wavelengths. The quiet Sun irradiates most of the energy in visible (white-light) wavelengths, to which our human eyes have developed the prime sensitivity during the evolution. Emission in extreme ultraviolet is dominant in the solar corona, because it is produced by ionized plasma in the coronal temperature range of ≈1-2 million K. Emissions in shorter wavelengths require higher plasma temperatures and thus occur during flares only. Flares also accelerate particles to nonthermal energies, which cause emission in hard X-rays, gamma-rays, and radio wavelengths, but to a highly variable degree.

2 The Solar Interior

The physical structure of the solar interior is mostly based on (1) theoretical models that are constrained by global quantities (age, radius, luminosity, total energy output; see Table 1), (2) by the measurement of global oscillations (helioseismology), and (3) by the neutrino flux, which now puts for the first time constraints on elemental abundances in the solar interior, since the neutrino problem has been solved in the year 2001.

2.1 Standard Models

There are two types of models of the solar interior: (1) hydrostatic equilibrium models, and (2) time-dependent numerical simulations of the evolution of the Sun, starting from an initial gas cloud to its present state today, after ≈8% of the hydrogen has been burned into helium.

The standard hydrostatic model essentially calculates the radial run of temperature, pressure, and density that fulfill the conservation of mass, momentum, and energy in all internal spherical layers of the Sun, constrained by the boundary conditions of radius, temperature, and radiation output (luminosity) at the solar surface, the total mass, and the chemical composition. Furthermore, the *ideal gas law* and thermal equilibrium is assumed, and thus the radiation is close to that of an *ideal black body*. The solar radius has been measured by triangulation inside the solar system (e.g., during a Venus transit) and by radar echo measurements. The mass of the Sun has been deduced from the orbital motions of the planets (Kepler's laws) and from precise laboratory measurements of the gravitational constant. The solar luminosity is measured by the heat flux received at Earth. From these standard models, a central temperature of ≈ 15 million K, a central density of ≈ 150 g cm^{-3}, and a central pressure of 2.3×10^{17} dyne cm^{-2} has been inferred. Fine-tuning of the standard model is obtained by including convective transport and by varying the (inaccurately known) helium abundance.

2.2 Thermonuclear Energy Source

The source of solar energy was understood in the 1920s, when Hans Bethe, George Gamov, and Carl Von Weizsäcker identified the relevant nuclear chain reactions that generate solar energy. The main nuclear reaction is the transformation of hydrogen into helium, where 0.7% of the mass is converted into radiation (according to Einstein's energy equivalence, $E = mc^2$), the so-called *p-p chain*, which starts with the fusion of two protons into a nucleus of deuterium (^{2}He), and after chain reactions involving ^{3}He, ^{7}Be, and ^{7}Li produces helium (^{4}He),

$$\begin{aligned} p + p &\mapsto {}^2He + e^+ + \nu_e \\ {}^2He + p &\mapsto {}^3He + \gamma \\ {}^3He + {}^3He &\mapsto {}^4He + p + p \end{aligned}$$

or

$$\begin{aligned} {}^3He + {}^4He &\mapsto {}^7Be + \gamma \\ {}^7Be + e^- &\mapsto {}^7Li + \nu_e \\ {}^7Li + p &\mapsto {}^8Be + \gamma \mapsto {}^4He + {}^4He \end{aligned}$$

One can estimate the Sun's lifetime by dividing the available mass energy by the luminosity,

$$t_\odot \approx 0.1 \times 0.007\, m_\odot c^2 / L_\odot \approx 10^{10} \text{ years},$$

where we assumed that only about a fraction of 0.1 of the total solar mass is transformed, because only the innermost core of the Sun is sufficiently hot to sustain nuclear reactions.

An alternative nuclear chain reaction occurring in the Sun and stars is the *Carbon-Nitrogen-Oxygen (CNO)* cycle,

$$\begin{aligned} {}^{12}C + p &\mapsto {}^{13}N + \gamma \\ {}^{13}N &\mapsto {}^{13}C + e^+ + \nu_e \\ {}^{13}C + p &\mapsto {}^{14}N + \gamma \\ {}^{14}N + p &\mapsto {}^{15}O + \gamma \\ {}^{15}O &\mapsto {}^{15}N + e^+ + \nu_e \\ {}^{15}N + p &\mapsto {}^{12}C + {}^4He\,. \end{aligned}$$

The p-p chain produces 98.5% of the solar energy, and the CNO cycle the remainder, but the CNO-cycle is faster in stars that are more massive than the Sun.

2.3 Neutrinos

Neutrinos have extremely little interactions with matter, unlike photons, and thus most of the electronic neutrinos (ν_e), emitted by the fusion of hydrogen to helium in the central core, escape the Sun

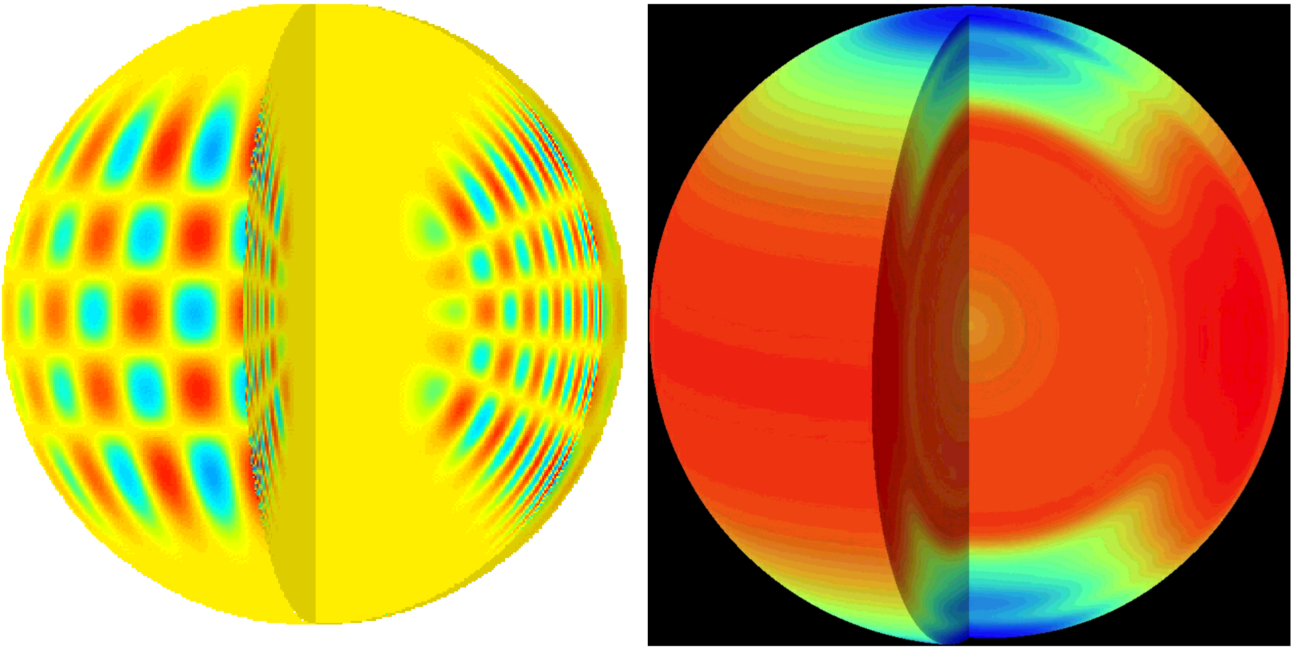

Figure 3: *Left:* A global acoustic p-mode wave is visualized: The radial order is $n = 14$, the angular degree is $l = 20$, the angular order is $m = 16$, and the frequency was measured to $\nu = 2935.88 \pm 0.1$ μHz with SoHO/MDI. The red and blue zones show displacement amplitudes of opposite sign. *Right:* The internal rotation rate is shown with a color code, measured with SoHO/MDI during 1996 May-1997 April. The red zone show the fastest rotation rates ($P \approx 25$ days), dark blue the slowest ($P \approx 35$ days). Note that the rotation rate varies in latitude differently in the radiative and convective zones (courtesy of SoHO/MDI and NASA).

without interactions and a very small amount is detected at Earth. Solar neutrinos have been detected since 1967, pioneered by Raymond Davis Jr. using a chlorine tank in the Homestake Gold Mine in South Dakota, but the observed count rate was about a third of the theoretically expected value, causing the puzzling *neutrino problem* that persisted for the next 35 years. However, Pontecorvo and Gribov predicted already in 1969 that low-energy solar neutrinos undergo a "personality disorder" on their travel to Earth and oscillate into other *atomic flavors* of *muonic neutrinos* (ν_μ) (from a process involving a muon particle) and *tauonic neutrinos* (ν_τ) (from a process involving a tauon particle), which turned out to be the solution of the *missing neutrino problem* for detectors that are only sensitive to the highest-energy (electronic) neutrinos, such as the Homestake chlorine tank, the gallium detectors *GALLEX* in Italy and *SAGE* in Russia. Only the *Kamiokande* and *Super-Kamiokande-I* pure-water experiments and the *Sudbury Neutrino Observatory* (*SNO*; Ontario, Canada) heavy-water experiments are somewhat sensitive to the muonic and tauonic neutrinos. It was the *SNO* that measured in 2001 for the first time all three *lepton flavors* and this way brilliantly confirmed the theory of *neutrino (flavor) oscillations*. Today, after the successful solution of the neutrino problem, the measured neutrino fluxes are sufficiently accurate to constrain the helium abundance and heavy element abundances in the solar interior.

2.4 Helioseismology

In the decade of 1960-1970, global oscillations were discovered on the solar surface in visible light, which became the field of *helioseismology*. Velocity oscillations were first measured by R. Leighton, and then interpreted in 1970 as standing sound waves in the solar convection zone by R. Ulrich, C. Wolfe, and J. Leibacher. These acoustic oscillations, also called *p-modes* (pressure-driven waves), are detectable from fundamental up to harmonic numbers of ≈ 1000, and are most conspicuous in dispersion diagrams, $\omega(k)$, where each harmonic shows up as a separate ridge, when the oscillation frequency (ω) is plotted as function of the wavelength λ (i.e., essentially the solar circumference divided by the harmonic number). Frequencies of the p-mode correspond to periods of $\approx$5 minutes. An example of a p-mode standing wave is shown in Fig. 3 (left), which appears like a standing wave on a drum skin. Each mode is characterized by the number of radial, longitudinal, and latitudinal nodes, corresponding to the radial quantum number n, the azimuthal number m, and the degree l of spherical harmonic functions. Since the density and temperature increase monotonically with depth inside the Sun, the sound speed varies as function of radial distance from Sun center. P-mode waves excited at the solar surface propagate downward and are refracted towards the surface, where the low harmonics penetrate very deep, while high harmonics are confined to the outermost layers of the solar interior. By measuring the frequencies at each harmonic, the sound speed can be inverted as function of the depth, and this way the density and temperature profile of the solar interior can be inferred and unknown parameters of theoretical standard models can be constrained, such as the abundance of helium and heavier elements. Exploiting the Doppler effect, frequency shifts of the p-mode oscillations can be used to measure the internal velocity rates as function of depth and latitude, as shown in Fig. 3 (right). A layer of rapid change in the internal rotation rate was discovered this way at the bottom of the convection zone, the so-called *tachocline* (at 0.693 ± 0.002 solar radius, with a thickness of 0.039 ± 0.013 solar radius).

Besides the p-mode waves, *gravity waves* (*g-modes*), where buoyancy rather than pressure supplies the restoring force, are suspected in the solar core. These gravity waves are predicted to have long periods (hours) and very small velocity amplitudes, but have not yet been convincingly detected.

While *global helioseismology* detects p-modes as a pattern of standing waves that encompass the entire solar surface, local deviations of the sound speed can also be detected beneath sunspots and active regions, a diagnostic that is called *local helioseismology*. Near sunspots, p-modes are found to have oscillation periods in the order of 3 minutes, compared to 5 minutes in active region plages and quiet-Sun regions.

2.5 Solar Dynamo

The Sun is governed by a strong magnetic field (much stronger than those on planets), which is generated with a magnetic field strength of $B \approx 10^5$ G in the *tachocline*, the thin shear layer sandwiched between the radiative and the convective zone. Buoyant magnetic flux tubes rise through the convection zone (due to the *convective instability* obeying the *Schwartzschild criterion*) and emerge at the solar surface in active regions, where they form sunspots with magnetic field strengths of $B \approx 10^3$ G and coronal loops with field strengths of $B \approx 10^2$ at the photospheric footpoints, and $B \approx 10$ G in larger coronal heights. The differential rotation on the solar surface is thought to wind up the surface magnetic field, which then fragments under the magnetic stress, circulates meridionally to the poles, and reorients from the toroidally stressed state (with field lines oriented in East-West direction) at solar maximum into a poloidal dipole field (connecting the north with the south pole) in the solar minimum. This process is called the *solar dynamo*, which flips the magnetic polarity of the Sun every ≈ 11 years (the *solar cycle*), or returns to the same magnetic configuration every ≈ 22 years (the *Hale cycle*). The solar cycle controls the occurrence rate of all solar activity phenomena; from sunspot numbers, active regions, to flares, and *coronal mass ejections (CMEs).*

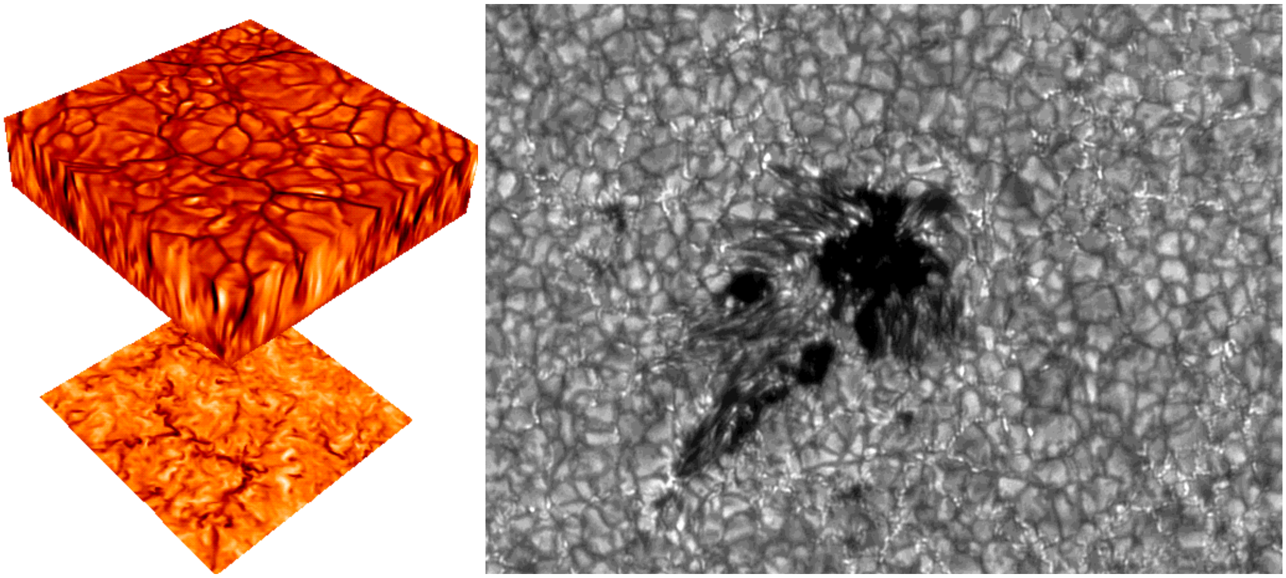

Figure 4: *Left:* Numerical simulation of cellular convection at the solar surface, performed by Fausto Cattaneo and Andrea Malagoli; *Right:* High-resolution observation of the granulation pattern in the solar photosphere. A granule has a typical size of 1000 km, representing the surface of an elementary convection cell. The large black area represents a sunspot, where the temperature is cooler than the surroundings. This image was taken by Tom Berger with the Swedish Solar Observatory.

3 The Photosphere

The photosphere is a thin layer at the solar surface that is observed in white light. The irradiance spectrum in Fig. 2 shows the maximum at visible wavelengths, which can be fitted with a *black-body spectrum* with a temperature of $T \approx 6400$ K at wavelengths of $\lambda \gtrsim 2000$ Å, which is the solar surface temperature. The photosphere is defined as the range of heights from which photons directly escape, which encompasses an optical depth range of $0.1 \lesssim \tau \lesssim 3$ and translates into a height range of $h \approx 300$ km for the visible wavelength range.

3.1 Granulation and Convection

The photospheric plasma is only partially ionized, there are less than 0.001 electrons per hydrogen atom at the photospheric temperature of $T = 6400$ K at $\lambda = 5000$ Å. These few ionized electrons come mostly from less abundant elements with a low ionization potential, such as magnesium, while hydrogen and helium are almost completely atomic. The magnetic field is *frozen in* to the gas under these conditions. However, the temperature is rapidly increasing below the photospheric surface, exceeding the hydrogen ionization temperature of $T = 11,000$ K at a depth of 50 km, where the the number of ionized electrons increases to 0.1 electrons per hydrogen atom, and the opacity increases by a similar factor. The high opacity of the partially ionized plasma impedes the heat flow. Moreover, a stratification with a temperature gradient steeper than an adiabatic gradient is unstable to convection (Schwartzschild criterion). Thus the partially-ionized photosphere of the Sun, as well as of other low-mass stars (with masses $m < 2m_{\odot}$) are therefore *convective.*

The observational manifestation of sub-photospheric convection is the granulation pattern (Fig. 4, right), which contains granules with typical sizes of ≈ 1000 km and lifetimes of $\tau \approx 7$ min. The subphotospheric gas flows up in the bright centers of granulation cells, cools then by radiating away some heat at the optically thin photospheric surface, and while cooling it becomes denser and flows

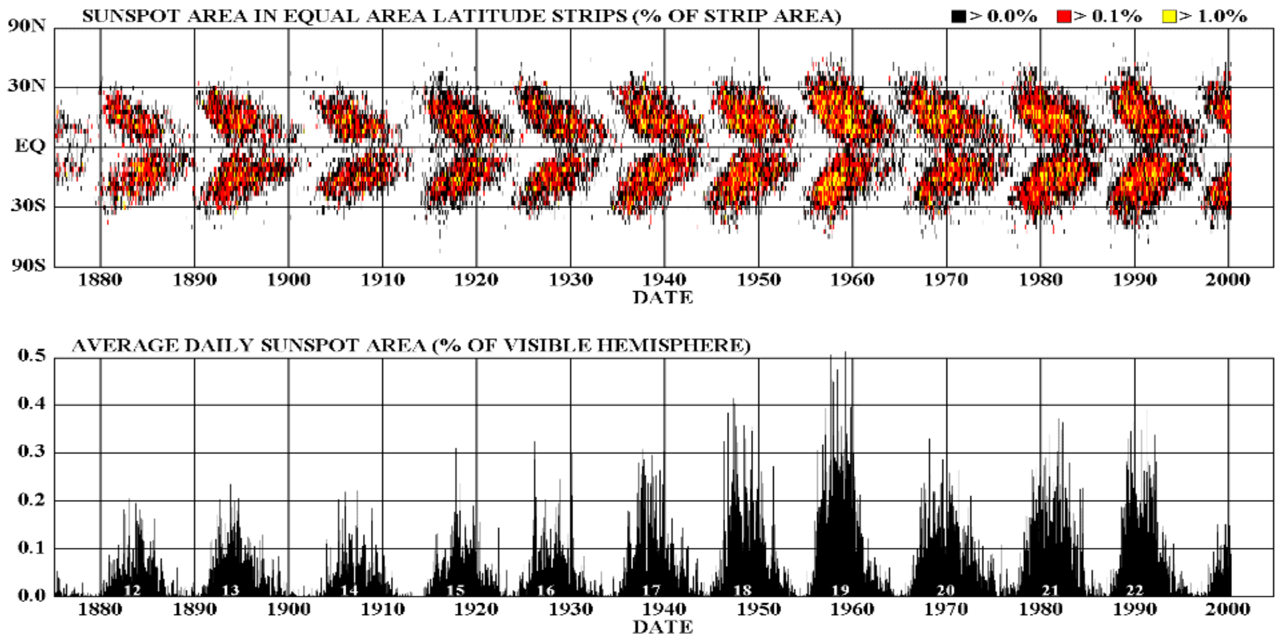

Figure 5: *Top:* Butterfly diagram of sunspot appearance, which marks the heliographic latitude of sunspot locations as function of time, during the solar cycles 12-23 (covering the years 1880-2000). *Bottom:* Sunspot area as function of time, which is a similar measure of the solar cycle activity as the sunspot number (courtesy of D. Hathaway and NASA/MSFC).

down in the intergranular lanes. This convection process can now be reproduced with numerical simulations that include hydrodynamics, radiative transfer, and atomic physics of ionization and radiative processes (Fig. 4, left). The convection process is also organized on larger scales, exhibiting cellular patterns on scales of ≈5,000-10,000 km (*mesogranulation*), and on scales of $\approx 20,000$ km (*supergranulation*).

3.2 Photospheric Magnetic Field

Most of what we know about the solar magnetic field is inferred from observations of the photospheric field, from the Zeeman effect of spectral lines in visible wavelengths (e.g., Fe 5250 Å). From 2D maps of the photospheric magnetic field strength we extrapolate the coronal 3D magnetic field, or try to trace the subphotospheric origin from emerging magnetic flux elements. The creation of magnetic flux is thought to happen in the tachocline at the bottom of the convection zone, from where it rises upward in form of buoyant magnetic flux tubes and emerges at the photospheric surface. The strongest fields emerge in sunspots, amounting to several kilogauss field strengths, and fields with strengths of several 100 G emerge also all over in active regions, often in form of a *leading sunspot* trailed by *following groups* of opposite magnetic polarity. Due to the convective motion, small magnetic flux elements that emerge in the center of granulation cells are then swept to the intergranular lanes, where often unresolved small concentrations are found, with sizes of less than a few 100 km. The flow velocities due to photospheric convection is of order ≈ 1 km s^{-1}. In the quiet Sun, away from active regions, the mean photospheric magnetic field amounts to a few Gauss.

3.3 Sunspots

Sunspots are the areas with the strongest magnetic fields, and therefore a good indicator of the solar activity (Fig. 5, bottom). The *butterfly diagram* shows that sunspots (or active regions) appear first at higher latitudes early in the solar cycle, and drift equatorward towards the end of the solar cycle (Fig. 5, top). Since all solar activity phenomena are controlled by the magnetic field, they have a similar solar cycle dependence as sunspots, such as the flare rate, active region area, global soft X-ray brightness, radio emission, etc. The appearance of dark sunspots lowers the total luminosity of the Sun only by about 0.15% at sunspot maximum, and thus the variation of the sunlight has a negligible effect on the Earth's climate. The variation of the EUV emission, which affects the ionization in the Earth's ionosphere, however, has a more decisive impact on the Earth's climate.

An individual sunspot consists of a very dark central *umbra*, surrounded by a brighter, radially striated *penumbra*. The darkness of sunspots is attributed to the inhibition of convective transport of heat, emitting only about 20% of the average solar heat flux in the umbra and being significantly cooler (≈ 4500 K) than the surroundings (≈ 6000 K). Their diameters range from 3600 km to 50,000 km and their lifetime ranges from a week to several months. The magnetic field in the umbra is mostly vertically oriented, but is strongly inclined over the penumbra, nearly horizontally. Current theoretical models explain the interlocking-comb structure of the filamentary penumbra with outward submerged field lines that are pumped down by turbulent, compressible convection of strong descending plumes.

Sunspots are used to trace the surface rotation, since Galileo in 1611. The average sidereal differential rotation rate is

$$\omega = 14.522 - 2.84 \ \sin^2 \Phi \quad \mathrm{deg/day} \ .$$

where Φ is the heliographic latitude. The rotation rate of an individual feature, however, can deviate from this average by a few percent, because it depends on the anchor depth to which the feature is rooted, since the solar internal differential rate varies radially (Fig. 3, right).

4 The Chromosphere and Transition Region

4.1 Basic Physical Properties

The chromosphere (from the Greek word $\chi\rho\omega\mu o\sigma$, color) is the lowest part of the solar atmosphere, extending to an average height of $\approx$2000 km above the photosphere. The first theoretical concepts conceived the chromosphere as a spherical layer around the solar surface (in the 1950s; Fig. 6, left), while later refinements included the diverging magnetic fields (canopies) with height (in the 1980s; Fig. 6, middle), and finally ended up with a very inhomogeneous mixture of cool gas and hot plasma, as a result of the extremely dynamic nature of chromospheric phenomena (in the 2000s; Fig. 6, right). According to hydrostatic standard models assuming *local thermodynamic equilibrium (LTE)*, the temperature reaches first a temperature minimum of $T = 4300$ K at a height of $h \approx 500$ km above the photosphere, and rises then suddenly to $\approx$10,000 K in the upper chromosphere at $h \approx 2000$ km, but the hydrogen density drops by about a factor of 10^6 over the same chromospheric height range. These hydrostatic models have been criticized because they neglect the magnetic field, horizontal inhomogeneities, dynamic processes, waves, and non-LTE conditions.

Beyond the solar limb (without having the photosphere in the background), the chromospheric spectrum is characterized by emission lines, while these lines appear dark on the disk as a result of photospheric absorption. The principal lines of the photospheric spectrum are called the Fraunhofer lines, including, e.g., hydrogen lines (H I; with the Balmer series Hα (6563 Å, Hβ 4861 Å, Hγ 4341 Å, Hδ 4102 Å), calcium lines (Ca II; K 3934 Å, H 3968 Å), and helium lines (He I; D_3 5975 Å).

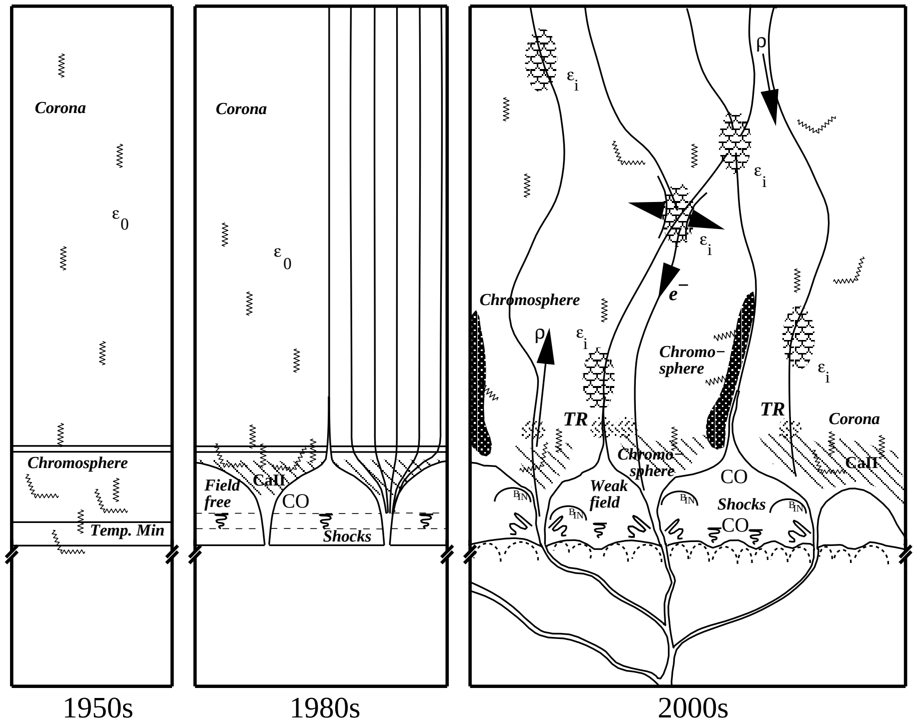

Figure 6: Cartoon of geometric concepts of the solar chromosphere, transition region, and corona: gravitationally stratified layers in the 1950s (*left*), vertical fluxtubes with chromospheric canopies in the 1980s (*middle*), and a fully inhomogeneous mixing of photospheric, chromospheric, and coronal zones by dynamic processes such as heated upflows, cooling downflows, intermittent heating (ε), nonthermal electron beams (e), field line motions and reconnections, emission from hot plasma, absorption and scattering in cool plasma, acoustic waves, and shocks (*right*) (courtesy of Carolus J. Schrijver).

4.2 Chromospheric Dynamic Phenomena

The appearance and finestructure of the chromosphere varies enormously depending on which spectral line, wavelength, and line position (core, red wing, blue wing) is used, because of their sensitivity to different temperatures (and thus altitudes) and Doppler shifts (and thus velocity ranges). In the H and K lines of Ca II the chromospheric images show a bright *network* surrounding supergranulation cells, which coincide with the large-scale subphotospheric convection cells. In the Ca II K2 or in UV continuum lines (1600 Å), the network and internetwork appears grainier. The so-called *bright grains* have a high contrast in wavelengths that are sensitive to the temperature minimum (4300 K), with an excessive temperature of 30-360 K, and with spatial sizes of ≈1000 km. The *bright points* in the network are generally associated with magnetic elements that collide, which then heat the local plasma after magnetic reconnection. In the intranetwork, *bright grains* result from chromospheric oscillations that produce shock waves. There are also very thin spaghetti-like elongated fine structure visible in Hα spectroheliograms (Fig. 7, left), which are called *fibrils* around sunspots. More vertically oriented fine structure are called *mottles* on the disk, or *spicules* above the limb. *Mottles* appear as irregular threads, localized in groups around and above supergranules, at altitudes of 700-3000 km above the photosphere, with lifetimes of 12-20 min, and are apparently signatures of upward and downward motions of plasmas with temperatures of T =8000-15,000 K and velocities of v ≈5-10 km s^{-1}. *Spicules* (Fig. 7, right) are jet-like structures of plasma with temperatures of T ≈10,000 K that rise to a maximum height of $h \lesssim$ 10,000 km into the lower corona, with velocities of $v \approx 20$ km s^{-1}. They carry a maximum flux of 100 times the solar wind into the low corona. Recent numerical simulations by DePontieu and Erdélyi show that global (helioseismic) p-mode oscillations leak sufficient energy

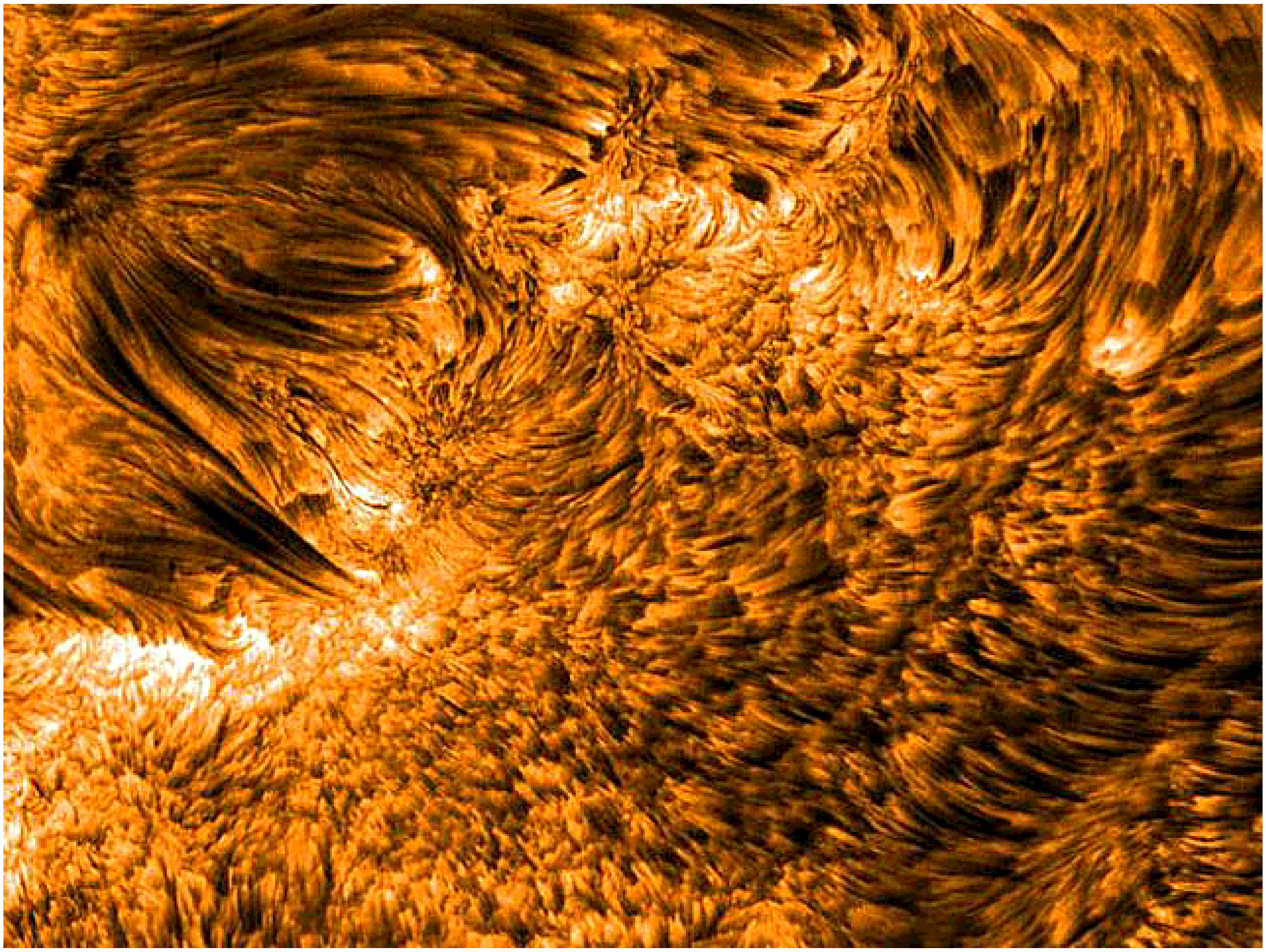

Figure 7: High-resolution image of Active Region 10380 on 2003-Jun-16, located near the limb, showing chromospheric spicules in the right half of the image. The image was taken with the *Swedish 1-meter Solar Telescope (SST)* on La Palma, Spain, using a tunable filter, tuned to the blue-shifted line wing of the Hα 6563 Å line. The spicules are jets of moving gas, flowing upward in the chromosphere with a speed of ≈ 15 km s^{-1}. The scale of the image is 65,000×45,000 km (courtesy of Bart DePontieu).

from the global resonant cavity into the chromosphere to power shocks that drive upward flows and form spicules. There is also the notion that *mottles*, *fibrils*, and *spicules* could be unified, being different manifestations of the same physical phenomenon at different locations (quiet Sun, active region, above the limb), in analogy to the unification of *filaments* (on the disk) and *prominences* (above the limb).

5 The Corona

It is customary to subdivide the solar corona into three zones, which all vary their size during the solar cycle: (1) active regions, (2) quiet-Sun regions, and (3) coronal holes.

5.1 Active regions

Active Regions are located in areas of strong magnetic field concentrations, visible as sunspot groups in optical wavelengths or magnetograms. Sunspot groups typically exhibit a strongly concentrated leading magnetic polarity, followed by a more fragmented trailing group of opposite polarity. Because of this bipolar nature active regions are mainly made up of closed magnetic field lines. Due to the permanent magnetic activity in terms of magnetic flux emergence, flux cancellation, magnetic reconfigurations, and magnetic reconnection processes, a number of dynamic processes such as plasma heating, flares, and CMEs occur in active regions. A consequence of plasma heating in the chromosphere are upflows into coronal loops, which give active regions the familiar appearance of numerous filled loops, which are hotter and denser than the background corona, producing bright emission in soft X-rays and extreme ultraviolet (EUV) wavelengths. In the EUV image shown in Fig. 8, active regions appear in white.

5.2 Quiet-Sun Regions

Historically, the remaining areas outside of active regions were dubbed *quiet Sun* regions. Today, however, many dynamic processes have been discovered all over the solar surface, so that the term *quiet Sun* is considered as a misnomer, only justified in relative terms. Dynamic processes in the quiet Sun range from small-scale phenomena such as network heating events, nanoflares, explosive events, bright points, and soft X-ray jets, to large-scale structures, such as transequatorial loops or coronal arches. The distinction between active regions and quiet-Sun regions becomes more and more blurred because most of the large-scale structures that overarch quiet-Sun regions are rooted in active regions. A good working definition is that quiet-Sun regions encompass all closed magnetic field regions (excluding active regions), which demarcates the quiet Sun territory from coronal holes (that encompass open magnetic field regions).

5.3 Coronal Holes

The northern and southern polar zones of the solar globe have generally been found to be darker than the equatorial zones during solar eclipses. Max Waldmeier thus dubbed those zones as *coronal holes* (i.e., “Koronale Löcher” in german). Today it is fairly clear that these zones are dominated by open magnetic field lines, that act as efficient conduits for flushing heated plasma from the corona into the solar wind, whenever they are fed by chromospheric upflows at their footpoints. Because of this efficient transport mechanism, coronal holes are empty of plasma most of the time, and thus appear much darker than the quiet Sun, where heated plasma flowing upward from the chromosphere remains trapped, until it cools down and precipitates back to the chromosphere. A coronal hole is visible in Fig. 8 at the north pole, where the field structures point radially away from the Sun and show a cooler temperature ($T \lesssim 1.0$ MK; dark blue in Fig. 8) than the surrounding Quiet-Sun regions.

5.4 Hydrostatics of Coronal Loops

Coronal loops are curvi-linear structures aligned with the magnetic field. The cross-section of a loop is essentially defined by the spatial extent of the heating source, because the heated plasma distributes along the coronal magnetic field lines without cross-field diffusion, since the thermal pressure is much less than the magnetic pressure in the solar corona. The solar corona consists of many thermally isolated loops, where each one has its own gravitational stratification, depending on its plasma temperature. A useful quantity is the *hydrostatic pressure scale height* λ_p, which depends only on the electron temperature T_e,

$$\lambda_p(T_e) = \frac{2k_B T_e}{\mu m_H g_\odot} \approx 47,000 \left(\frac{T_e}{1 \text{ MK}}\right) \qquad (\text{km}) \ .$$

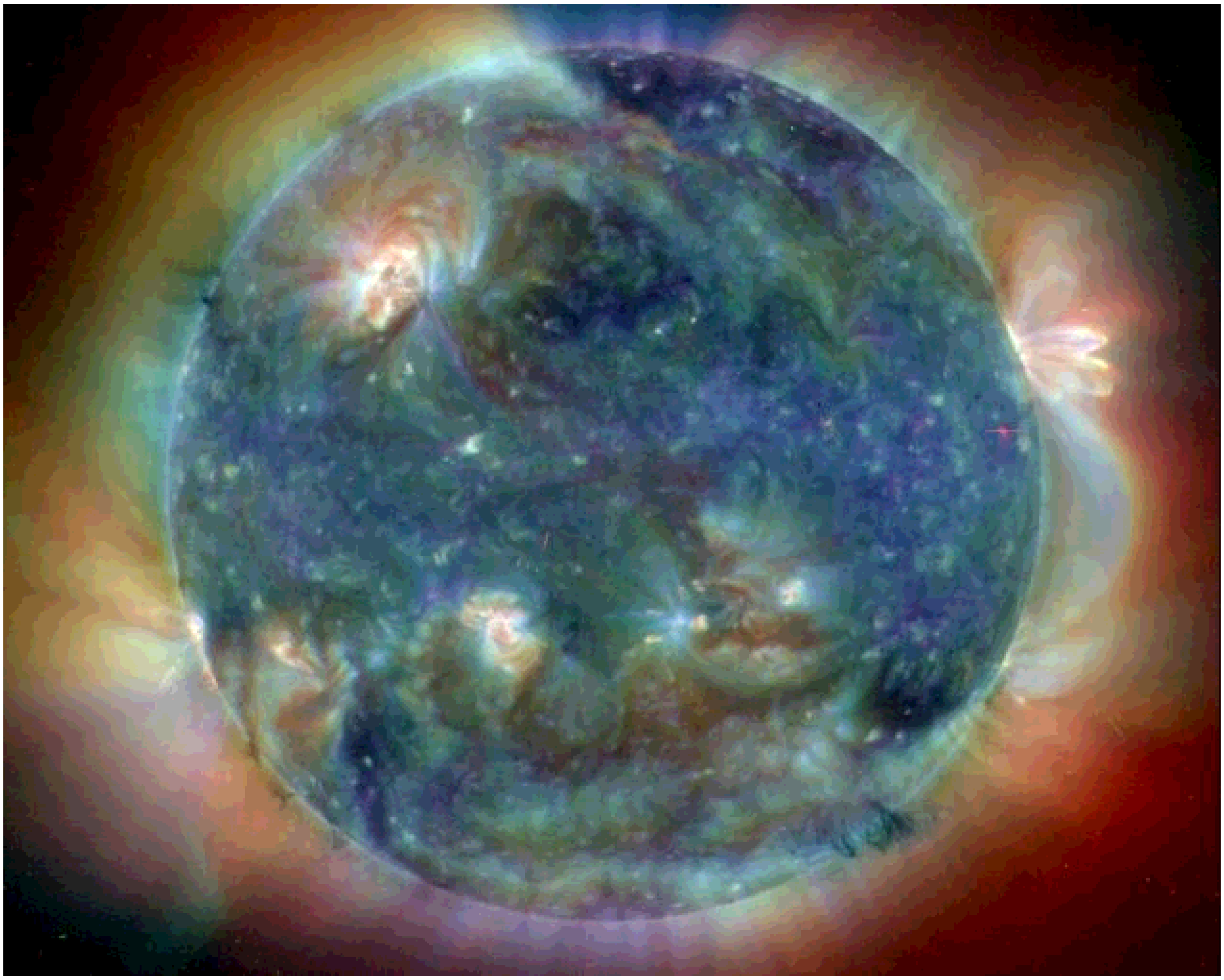

Figure 8: The multi-temperature corona, recorded with the EIT instrument on board the SoHO spacecraft. The representation shown here is a false-color composite of three images all taken in extreme ultraviolet light. Each individual image highlights a different temperature regime in the upper solar atmosphere and was assigned a specific color; red at 2 million, green at 1.5 million, and blue at 1 million degrees K. The combined image shows active regions in white color (according to Newton's law of color addition), because they contain many loops with different temperatures. Also nested regions above the limb appear in white, because they contain a multitude of loops with different temperatures along a line-of-sight, while isolated loops on the disk show a specific color according to their intrinsic temperature (courtesy of EIT/SoHO and NASA).

Observing the solar corona in soft X-rays or EUV, which are both optically thin emission, the line-of-sight integrated brightness intercepts many different scale heights, leading to a hydrostatic weighting bias towards systematically hotter temperatures in larger altitudes above the limb. The observed height dependence of the density needs to be modeled with a statistical ensemble of multi-hydrostatic loops. Measuring a density scale height of a loop requires careful consideration of projection effects, loop plane inclination angles, cross-sectional variations, line-of-sight integration, and the instrumental response functions. Hydrostatic solutions have been computed from the energy balance between the heating rate, the radiative energy loss, and the conductive loss. The major unknown quantity is the spatial heating function, but analysis of loops in high-resolution images indicate that the heating function is concentrated near the footpoints, say at altitudes of $h \lesssim 20,000$ km. Of course, a large number of coronal loops are found to be not in hydrostatic equilibrium, while nearly hydrostatic loops

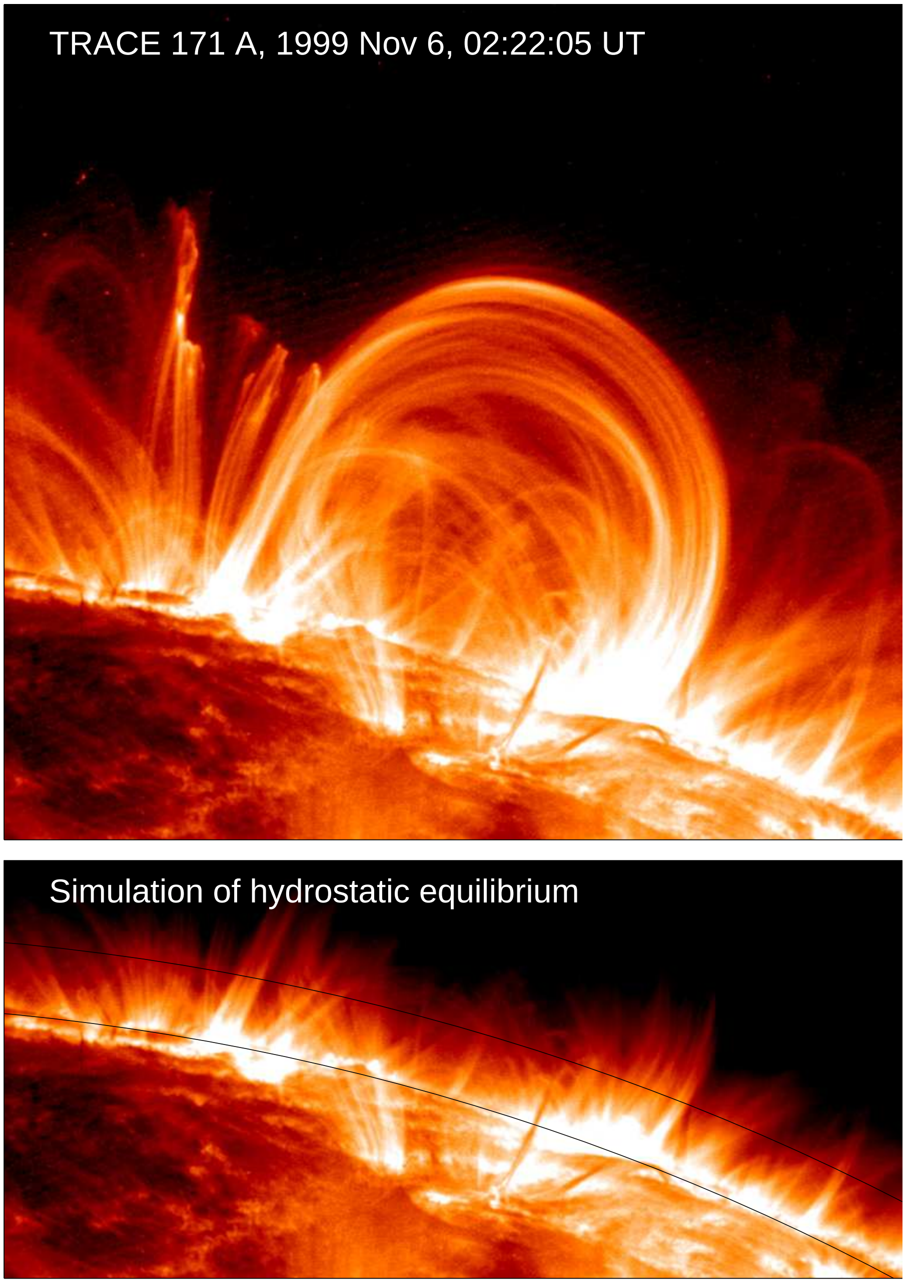

Figure 9: An active region with many loops that have an extended scale height of $\lambda_p/\lambda_T \lesssim 3-4$ (left panel) has been scaled to the hydrostatic thermal scale height of $T = 1$ MK (right panel). The pressure scale height of the 1 MK plasma is $\lambda_T = 47,000$ km, but the observed flux is proportional to the emission measure ($F \mapsto EM \mapsto n_e^2$), which has the half pressure scale height $\lambda_T/2 = 23,000$ km.

have been found preferentially in the quiet corona and in older dipolar active regions. An example of an active region (recorded with the *Transition Region and Coronal Explorer (TRACE)* about 10 hours after a flare) is shown in Fig. 9, which clearly shows super-hydrostatic loops where the coronal plasma is distributed over up to 4 times larger heights than expected in hydrostatic equilibrium (Fig. 9, bottom).

5.5 Dynamics of the Solar Corona

Although the Sun appears as lifeless and unchanging to our eyes, except for the monotonic rotation that we can trace from the sunspot motions, there are actually a lot of vibrant dynamic plasma processes continuously happening in the solar corona, which can be detected mainly in EUV and soft X-rays. There is currently a paradigm shift stating that most of the apparently static structures seen in the corona are probably controlled by plasma flows and intermittent heating. It is, however, not easy to measure and track these flows with our remote sensing methods, like the apparently motionless rivers seen from an airplane. For slow flow speeds, so-called *laminar flows*, there is no feature to track, while turbulent flows may be easier to detect, because they produce whirls and vortices that can be tracked. A similar situation happens in the solar corona. Occasionally a moving plasma blob is detected in a coronal loop that can be used as a tracer. Most of the flows in coronal loops seem to be subsonic (like laminar flows) and thus featureless. Occasionally we observe turbulent flows, which clearly reveal motion, especially when cool and hot plasma becomes mixed by turbulence and thus yields contrast by emission and absorption in a particular temperature filter. Motion can also be detected with Doppler shift measurements, but this yields only the flow component along the line-of-sight. There is increasing evidence that flows are ubiquitous in the solar corona.

There are a number of theoretically expected dynamic processes. For instance, loops at coronal temperatures are thermally unstable when the radiative cooling time is shorter than the conductive cooling time, or when the heating scale height falls below one-third of a loop half length. Recent observations show ample evidence for the presence of flows in coronal loops, as well as evidence for impulsive heating with subsequent cooling, rather than a stationary hydrostatic equilibrium. High-resolution observations of coronal loops reveal that many loops have a super-hydrostatic density scale height, far in excess of hydrostatic equilibrium solutions (Fig. 9, top). Time-dependent hydrodynamic simulations are still in a very exploratory phase and hydrodynamic modeling of the transition region, coronal holes, and the solar wind remains challenging due to the number of effects that can not easily be quantified by observations, such as unresolved geometries, inhomogeneities, time-dependent dynamics, and MHD effects.

The coronal plasma is studied with regard to hydrostatic equilibria in terms of fluid mechanics (*hydrostatics*), with regard to flows in terms of fluid dynamics (*hydrodynamics*), and including the coronal magnetic field in terms of *magneto-hydrodynamics (MHD)*. The coronal magnetic field has many effects on the hydrodynamics of the plasma. It can play a passive role in the sense that the magnetic geometry does not change (e.g., by channeling particles, plasma flows, heat flows, and waves along its field lines, or by maintaining a thermal insulation between the plasmas of neighboring loops or fluxtubes). On the other hand, the magnetic field can play an active role (where the magnetic geometry changes), such as exertion of a Lorentz force on the plasma, build-up and storage of nonpotential energy, triggering an instability, changing the topology (by various types of magnetic reconnection), and accelerating plasma structures (filaments, prominences, CMEs).

5.6 The Coronal Magnetic Field

The solar magnetic field controls the dynamics and topology of all coronal phenomena. Heated plasma flows along magnetic field lines and energetic particles can only propagate along magnetic field lines. Coronal loops are nothing other than conduits filled with heated plasma, shaped by the geometry of the coronal magnetic field, where cross-field diffusion is strongly inhibited. Magnetic field lines take on the same role for coronal phenomena as do highways for street traffic. There are two different magnetic zones in the solar corona that have fundamentally different properties: open-field

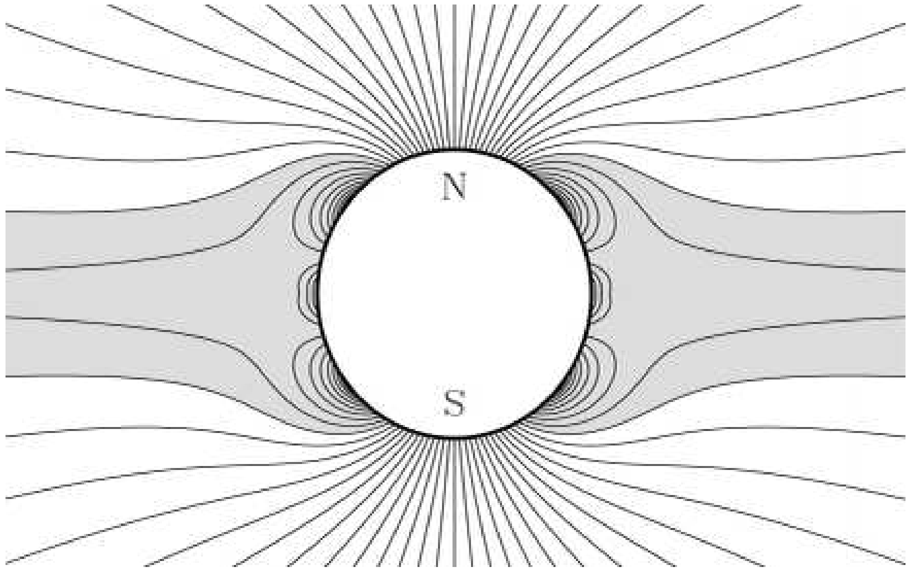

Figure 10: The global coronal magnetic field can be subdivided into open-field regions (mostly near the north and south pole regions) and into closed-field regions (mostly in latitudes of $\Phi \lesssim 70^0$). Tha analytical magnetic field model shown here, a multipole-current sheet coronal model of Banaszkiewicz, approximately outlines the general trends. The high-speed solar wind originates and leaves the Sun in the unshaded volume.

and closed-field regions. Open-field regions (white zones above the limb in Fig. 10), which always exist in the polar regions, and sometimes extend towards the equator, connect the solar surface with the interplanetary field and are the source of the *fast solar wind* (≈ 800 km s^{-1}). A consequence of the open-field configuration is efficient plasma transport out into the heliosphere, whenever chromospheric plasma is heated at the footpoints. Closed-field regions (grey zones in Fig. 10), in contrast, contain mostly closed field lines in the corona up to heights of about one solar radius, which open up at higher altitudes and connect eventually to the heliosphere, but produce a *slow solar wind* component of ≈ 400 km s^{-1}. It is the closed-field regions that contain all the bright and overdense coronal loops, produced by filling with chromospheric plasma that stays trapped in these closed field lines. For loops reaching altitudes higher than about one solar radius, plasma confinement starts to become leaky, because the thermal plasma pressure exceeds the weak magnetic field pressure that decreases with height (plasma-β parameter < 1).

The magnetic field on the solar surface is very inhomogeneous. The strongest magnetic field regions are in sunspots, reaching field strengths of $B = 2000 - 3000$ G. Sunspot groups are dipolar, oriented in an east-west direction (with the leading spot slightly closer to the equator) and with opposite leading polarity in both hemispheres, reversing every 11-year cycle (*Hale's laws*). Active regions and their plages comprise a larger area around sunspots, with average photospheric fields of $B \approx 100 - 300$ G, containing small-scale pores with typical fields of $B \approx 1000$ G. The background magnetic field in the quiet Sun and in coronal holes has a net field of $B \approx 0.1 - 0.5$ G, while the absolute field strengths in resolved elements amount to $B = 10 - 50$ G. Our knowledge of the solar magnetic field is mainly based on measurements of Zeeman splitting in spectral lines, while the coronal magnetic field is reconstructed by extrapolation from magnetograms at the lower boundary, using a potential or force-free field model. The extrapolation through the chromosphere and transition region is, however, uncertain due to unknown currents and non-force-free conditions. The fact that coronal loops exhibit generally much less expansion with height than potential-field models underscores the inadequacy of potential-field extrapolations. Direct measurements of the magnetic field in coronal heights are still in their infancy.

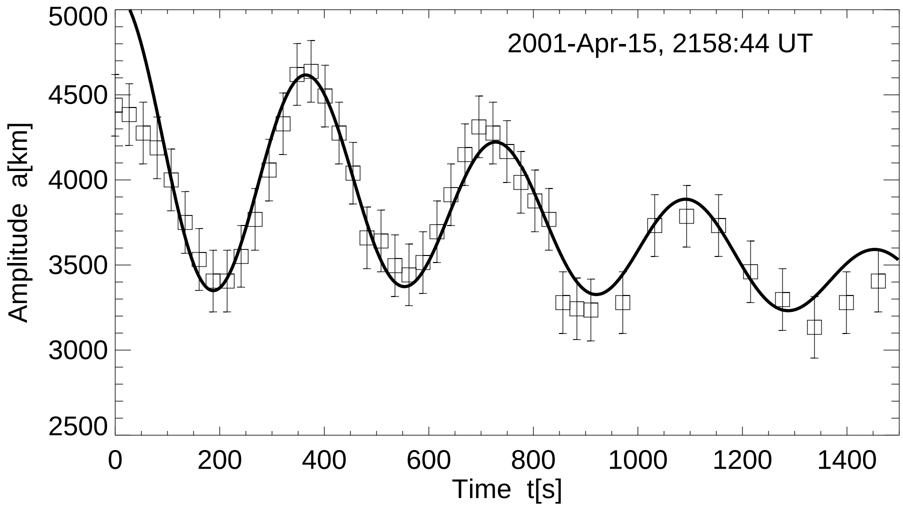

Figure 11: The transverse amplitude of a kink-mode oscillation measured in one loop of a postflare loop arcade observed with TRACE on 2001-Apr-15, 21:58:44 UT. The amplitudes are fitted by a damped sine plus a linear function, $a(t) = a_0 + a_1 \sin(2\pi * (t - t_0)/P) \exp(-t/\tau_D) + a_2 * t$, with a period of $P = 365$ s and a damping time of $\tau_D = 1000$ s (courtesy of Ed DeLuca and Joseph Shoer).

5.7 MHD Oscillations of Coronal Loops

Similarly to the discovery of helioseismology four decades ago, it was recently discovered that also the solar corona contains an impressively large ensemble of plasma structures that are capable of producing sound waves and harmonic oscillations. Thanks to the high spatial resolution, image contrast, and time cadence capabilities of the *Solar and Heliospheric Observatory (SoHO)* and TRACE spacecraft, oscillating loops, prominences, or sunspots, and propagating waves have been identified and localized in the corona and transition region, and studied in detail since 1999. These new discoveries established a new discipline that became known as *coronal seismology*. While the theory of MHD oscillations was developed several decades earlier, only the new imaging observations provide diagnostics on length scales, periods, damping times, and densities that allow a quantitative application of the theoretical dispersion relations of MHD waves. The theory of MHD oscillations has been developed for homogeneous media, single interfaces, slender slabs, and cylindrical fluxtubes. There are four basic speeds in fluxtubes: (1) the Alfvén speed $v_A = B_0/\sqrt{4\pi\rho_0}$, (2) the sound speed $c_s = \sqrt{\gamma p_0/\rho_0}$, (3) the cusp or tube speed $c_T = (1/c_s^2 + 1/v_A^2)^{-1/2}$, and (4) the kink or mean Alfvén speed $c_k = [(\rho_0 v_A^2 + \rho_e v_{Ae}^2)/(\rho_0 + \rho_e)]^{1/2}$. For coronal conditions, the dispersion relation reveals a slow-mode branch (with acoustic phase speeds) and a fast-mode branch of solutions (with Alfvén speeds). For the fast-mode branch, a symmetric (sausage) mode and an asymmetric (kink) mode can be distinguished. The fast kink mode produces transverse amplitude oscillations of coronal loops which have been detected with TRACE (Fig. 11), having periods in the range of P=2$-$10 min, and can be used to infer the coronal magnetic field strength, thanks to its non-dispersive nature. The fast sausage mode is highly dispersive and is subject to a long-wavelength cutoff, so that standing wave oscillations are only possible for thick and high-density (flare and postflare) loops, with periods in the range of P$\approx$1 s to 1 min. Fast sausage-mode oscillations with periods of P$\approx$10 s have recently been imaged for the first time with the Nobeyama radioheliograph, while there exist numerous earlier reports on non-imaging detections with periods of P$\approx$0.5$-$5 s. Finally, slow-mode acoustic oscillations have been detected in flare-like loops with SUMER, having periods in the range of P$\approx 5 - 30$ min. All loop oscillations observed in the solar corona have been found to be subject to strong damping, typically with decay times of only $1-2$ periods. The relevant damping mechanisms are resonant

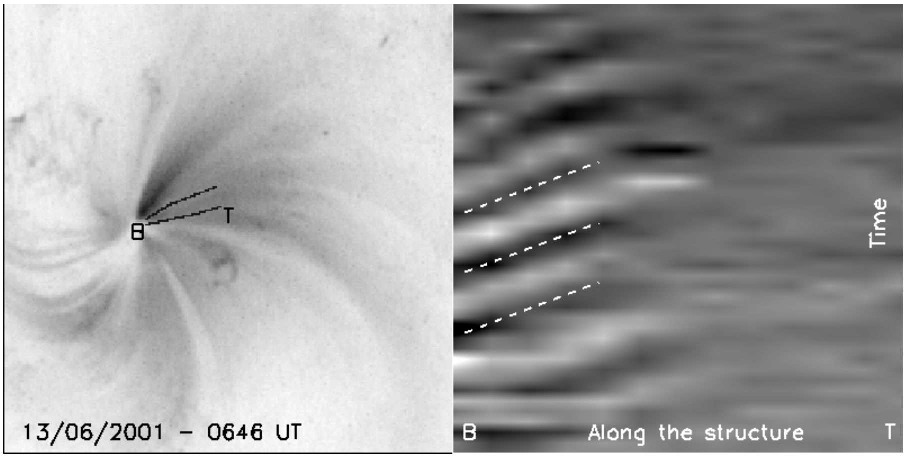

Figure 12: TRACE 171 Å observation of a slow-mode (acoustic) wave recorded on 2001 June 13, 06:46 UT. *Left:* the diverging fan-like loop structures emerge near a sunspot, where the acoustic waves are launched and propagate upward. *Right:* a running difference plot is shown for the loop segment marked in the left frame, with time running upward in the plot. Note the diagonal pattern which indicates propagating disturbances (courtesy of Ineke De Moortel).

absorption for fast-mode oscillations (or alternatively phase mixing, although requiring an extremely low Reynolds number), and thermal conduction for slow-mode acoustic oscillations. Quantitative modeling of coronal oscillations offer exciting new diagnostics on physical parameters.

5.8 MHD Waves in Solar Corona

In contrast to standing modes (with fixed nodes), also *propagating MHD waves* (with moving nodes) have been discovered in the solar corona recently. Propagating MHD waves result mainly when disturbances are generated impulsively, on time scales faster than the Alfvénic or acoustic travel time across a structure.

Propagating slow-mode MHD waves (with acoustic speed) have been recently detected in coronal loops with TRACE and SoHO/EIT (Fig. 12), usually being launched with 3-minute periods near sunspots, or with 5-minute periods in plage regions. These acoustic waves propagate upward from a loop footpoint and are quickly damped, and have never been detected in downward direction at the opposite loop side. Propagating fast-mode MHD waves (with Alfvénic speeds) have recently been discovered in a loop in optical (SECIS eclipse) data, as well as in (Nobeyama) radio images.

Besides from coronal loops, slow-mode MHD waves have also been detected in plumes in open field regions in coronal holes, while fast-mode MHD waves have not yet been detected in open field structures. However, spectroscopic observations of line broadening in coronal holes provide strong support for the detection of Alfvén waves, based on the agreement with the theoretically predicted height-dependent scaling between line broadening and density, $\Delta v(h) \propto n_e(h)^{-1/4}$.

The largest manifestation of propagating MHD waves in the solar corona are global waves that spherically propagate after a flare and/or CME over the entire solar surface. These global waves were discovered earlier in Hα, called *Moreton waves*, and recently in EUV, called *EIT waves* (Fig. 13), usually accompanied with a coronal dimming behind the wave front, suggesting evacuation of coronal plasma by the CME. The speed of Moreton waves is about three times faster than that of EIT waves, which still challenges dynamic MHD models of CMEs.

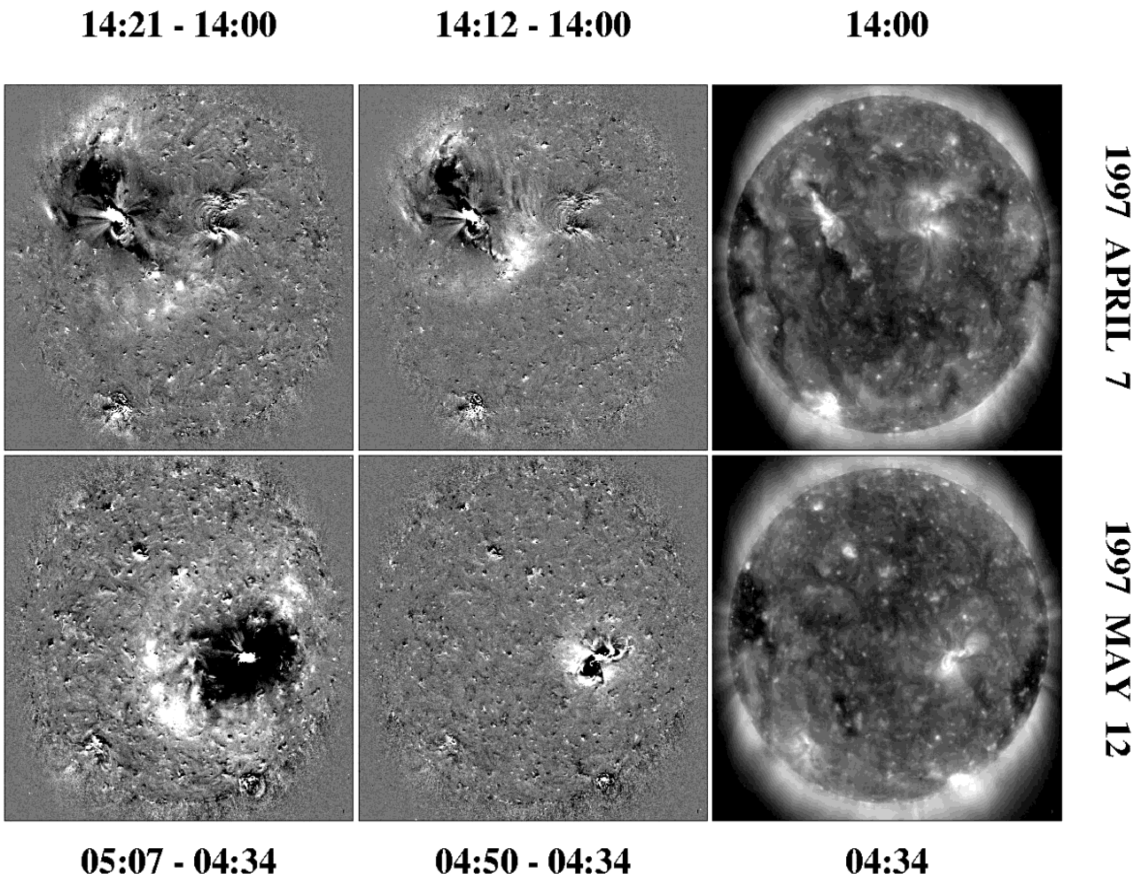

Figure 13: Two global wave events observed with SoHO/EIT 195 Å, on 1997 Apr 7 (top row) and 1997 May 12 (bottom row). The intensity images (right) were recorded before the eruption, while the difference images (left an middle) show differences between the subsequent images, enhancing emission measure increases (white areas) and dimming (black areas) (courtesy of Yi-Ming Wang).

5.9 Coronal Heating

When Bengt Edlén and Walter Grotrian identified Fe IX (nine-times ionized iron) and Ca XIV (fourteen-times ionized calcium) lines in the solar spectrum in 1943, a coronal temperature of $T \approx 1$ MK was first inferred from the formation temperature of these highly ionized atoms. A profound consequence of this measurement is the implication that the corona then consists of a fully ionized hydrogen plasma. Comparing this coronal temperature with the photospheric temperature of 6400 K, we are confronted with the puzzle of how the 200 times hotter coronal temperature can be maintained, the so-called *coronal heating problem*. Of course, there is also a *chromospheric heating problem* and a *solar wind heating problem*. If only thermal conduction were at work, the temperature in the corona should steadily drop down from the chromospheric value with increasing distance, according to the second law of thermodynamics. Moreover, since we have radiative losses by EUV emission, the corona would just cool off in matter of hours to days, if the plasma temperature could not be maintained continuously by some heating source.

The coronal heating problem has been narrowed down by substantial progress in theoretical modeling with MHD codes, new high-resolution imaging with the SXT (*Yohkoh Soft X-ray Telescope*), EIT (*SoHO Extreme-ultraviolet Imaging Telescope*) and TRACE (*Transition Region and Coronal Explorer*) telescopes, and with more sophisticated data analysis using automated pattern recognition

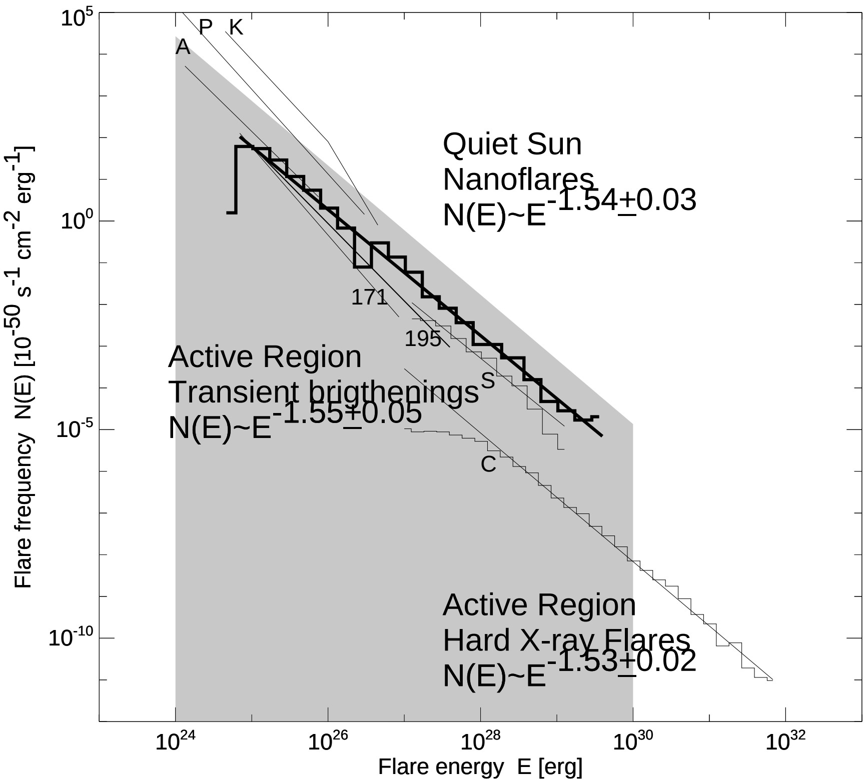

Figure 14: Compilation of frequency distributions of thermal energies from nanoflare statistics in the quiet Sun, active region transient brightenings, and hard X-ray flares. The overall slope of the synthesized nanoflare distribution, $N(E) \propto E^{-1.54\pm0.03}$, is similar to that of transient brightenings and hard X-ray flares. The grey area indicates the coronal heating requirement of $F = 3 \times 10^5$ erg cm^{-2} s^{-1} for quiet-Sun regions. Note that the observed distribution of nanoflare energies, which only includes the radiative losses, accounts for $\approx 1/3$ of the heating rate requirement of the Quiet Sun.

codes. The total energy losses in the solar corona range from $F = 3 \times 10^5$ erg cm^{-2} s^{-1} in quiet-Sun regions to $F \approx 10^7$ erg cm^{-2} s^{-1} in active regions. two main groups of DC (*Direct Current*) and AC (*Alternating Current*) models, which involve as a primary energy source chromospheric footpoint motion or upward leaking Alfvén waves, which are dissipated in the corona by magnetic reconnection, current cascades, MHD turbulence, Alfvén resonance, resonant absorption, or phase mixing. There is also strong observational evidence for solar wind heating by cyclotron resonance, while velocity filtration seems not to be consistent with EUV data. Progress in theoretical models has mainly been made by abandoning homogeneous fluxtubes, but instead including gravitational scale heights and more realistic models of the transition region, and taking advantage of numerical simulations with 3D MHD codes (e.g., see B. Gudiksen and A. Nordlund). From the observational side we can now unify many coronal small-scale phenomena with flare-like characteristics, subdivided into microflares (in soft X-rays) and nanoflares (in EUV) solely by their energy content. Scaling laws of the physical parameters corroborate their unification. They provide a physical basis to understand the frequency distributions of their parameters and allow estimation of their energy budget for coronal heating. Synthesized data sets of microflares and nanoflares in EUV and soft X-rays have established that these impulsive small-scale phenomena match the radiative loss of the average quiet Sun corona (Fig. 14), which points to small-scale magnetic reconnection processes in the transition region and lower corona as primary heating sources.

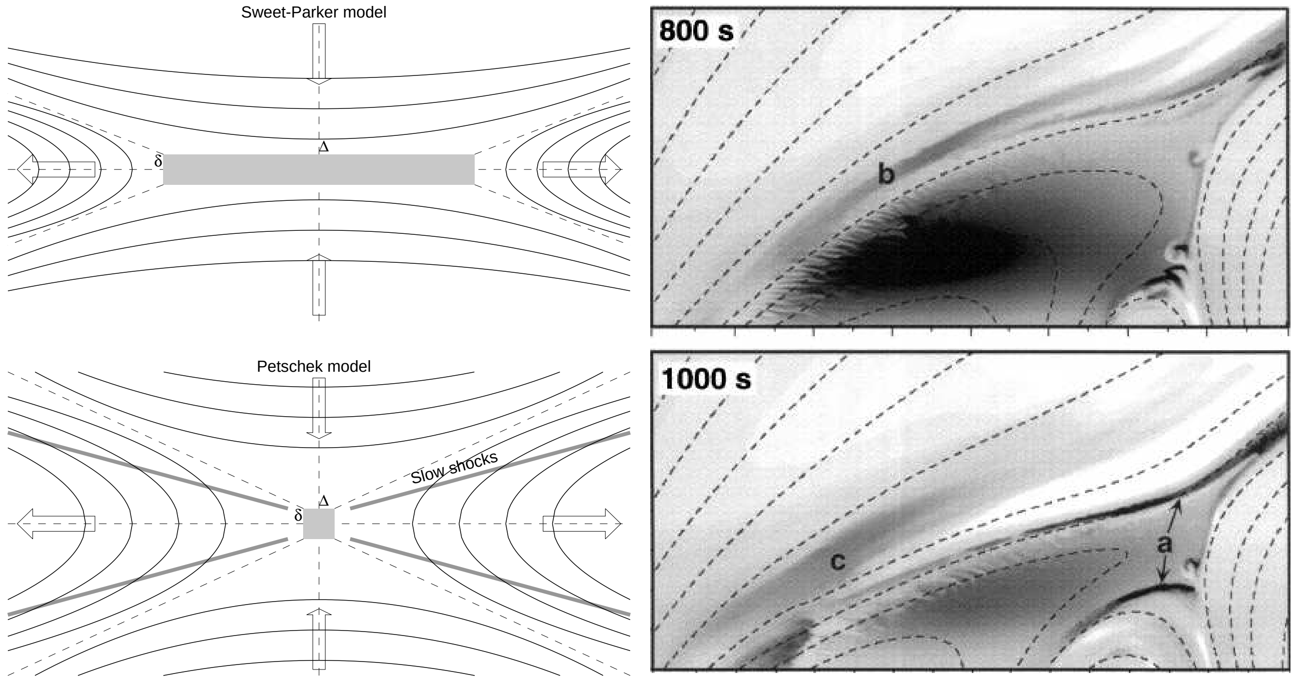

Figure 15: *Left:* Geometry of the Sweet−Parker (top) and Petschek reconnection model (bottom). The geometry of the diffusion region (grey box) is a long thin sheet ($\Delta \gg \delta$) in the Sweet−Parker model, but much more compact ($\Delta \approx \delta$) in the Petschek model. The Petschek model also considers slow-mode MHD shocks in the outflow region. *Right:* Numeric MHD simulation of a magnetic reconnection process in a sheared arcade. The greyscale represents the mass density difference ratio and the dashed lines shows the projected magnetic field lines in the vicinity of the reconnection region, at two particular times of the reconnection process. The location **a** corresponds to a thin compressed region along the slowly rising inner separatrix, **b** to a narrow downflow stream outside of the left outer separatrix, and **c** indicates a broader upflow that follows along the same field lines (courtesy of Judith Karpen).

6 Solar Flares and Coronal Mass Ejections

Rapidly-varying processes in the solar corona, which result from a loss of magnetic equilibrium, are called *eruptive phenomena*, such as *flares*, *CMEs*, or *eruptive filaments* and *prominences*. The fundamental process that drives all these phenomena is *magnetic reconnection*.

6.1 Magnetic Reconnection

The solar corona has dynamic boundary conditions: (1) The solar dynamo in the interior of the Sun constantly generates new magnetic flux from the bottom of the convection zone (i.e., the tachocline) which rises by buoyancy and emerges through the photosphere into the corona; (2) the differential rotation as well as convective motion at the solar surface continuously wrap up the coronal field; and (3) the connectivity to the interplanetary field has constantly to break up to avoid excessive magnetic stress. These three dynamic boundary conditions are the essential reasons why the coronal magnetic field is constantly stressed and has to adjust by restructuring the large-scale magnetic field by topological changes, called *magnetic reconnection* processes. Of course, such magnetic restructuring processes occur wherever magnetic stresses build up, such as in filaments, in twisted *sigmoid-shaped loops*, along *sheared neutral lines*, etc. Topological changes in the form of magnetic reconnection always liberate free nonpotential energy, which is converted into heating of plasma, acceleration of particles, and kinematic motion of coronal plasma. Magnetic reconnection processes can occur in a

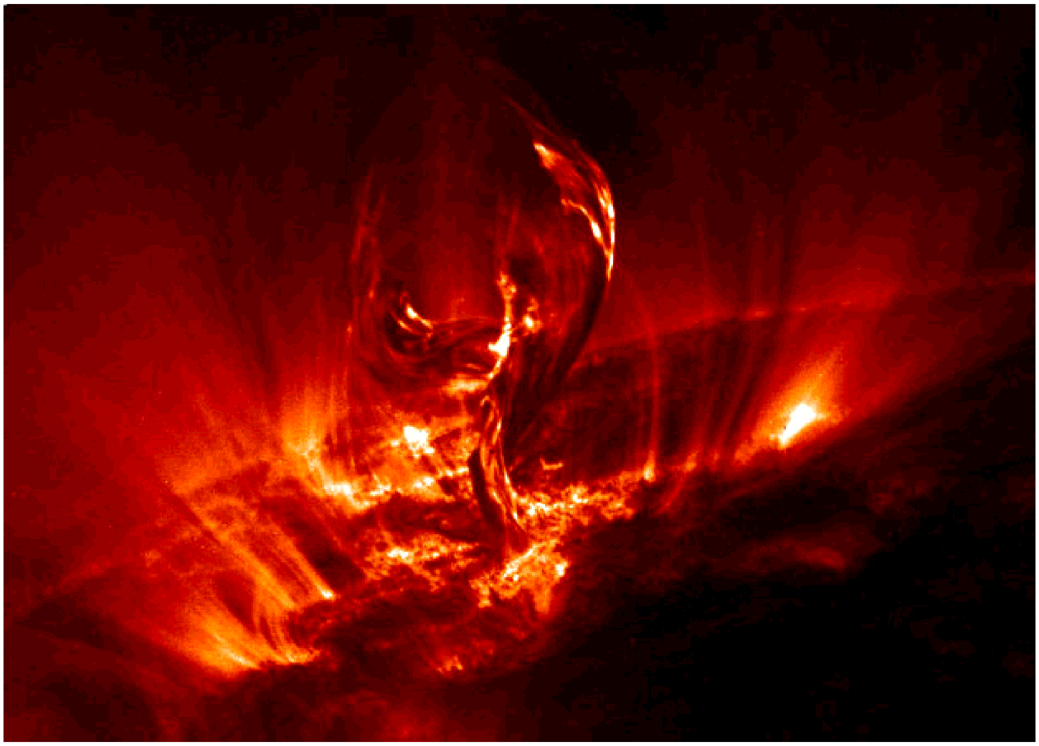

Figure 16: Erupting filament observed with TRACE at 171 Å on 2000-Jul-19, 23:30 UT, in Active Region 9077. The dark filament mass has temperatures around 20,000 K, while the hot kernels and threads contain plasma with temperatures of 1.0 MK or hotter. The erupting structure extends over a height of 75,000 km here (courtesy of TRACE and NASA).

slowly changing quasi-steady way, which may contribute to coronal heating (§ 5.9), but more often happen as sudden violent processes that are manifested as *flares* and *CMEs*.

Theory and numerical simulations of magnetic reconnection processes in the solar corona have been developed for steady 2D reconnection (Fig. 15, left), bursty 2D reconnection, and 3D reconnection. Only steady 2D reconnection models can be formulated analytically, which provide basic relations for inflow speed, outflow speed, and reconnection rate, but represent oversimplifications for most (if not all) observed flares. A more realistic approach seems to be bursty 2D reconnection models (Fig. 15, right), which involve the tearing-mode and coalescence instability and can reproduce the sufficiently fast temporal and small spatial scales required by solar flare observations. The sheared magnetic field configurations and the existence or coronal and chromospheric nullpoints, which are now inferred more commonly in solar flares, require ultimately 3D reconnection models, possibly involving nullpoint coalescence, spine reconnection, fan reconnection, and separator reconnection. Magnetic reconnection operates in two quite distinct physical parameter domains: in the chromosphere during magnetic flux emergence, magnetic flux cancellation, and so-called explosive events, and under coronal conditions during microflares, flares, and CMEs.

6.2 Filaments and Prominences

Key elements in triggering flares and/or CMEs are *erupting filaments*. A filament is a current system above a magnetic neutral line that builds up gradually over days and erupts during a flare or CME process. The horizontal magnetic field lines overlying a neutral line (i.e., the magnetic polarity inversion line) of an active region are filled with cool gas (of chromospheric temperature), embedded

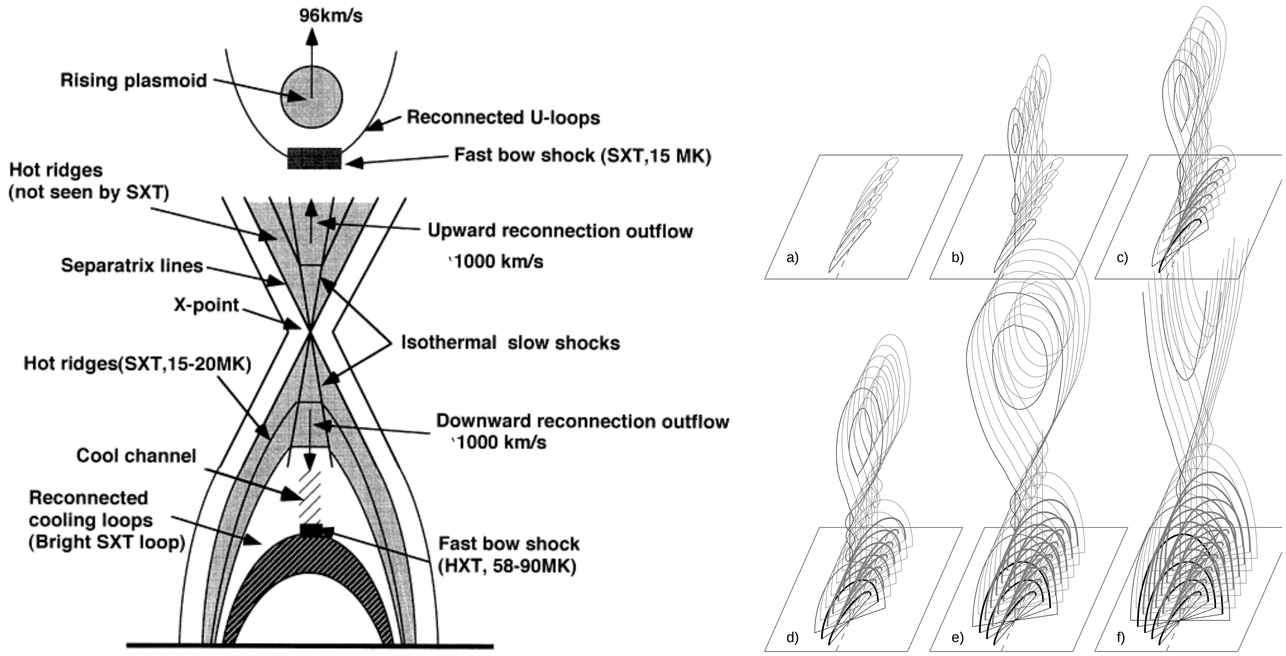

Figure 17: *Left:* A version of the standard 2D X-type reconnection model for two-ribbon flares, pioneered by Carmichael, Sturrock, Hirayama, and Kopp-Pneumann (CSHKP), which also includes the slow and fast shocks in the outflow region, the upward-ejected plasmoid, and the locations of the soft X-ray bright flare loops (courtesy of Saku Tsuneta). *Right:* 3D version of the two-ribbon flare model, based on the observed evolution during the Bastille-Day 2000-Jul-14 flare: *(a)* low-lying, highly sheared loops above the neutral line first become unstable; *(b)* after loss of magnetic equilibrium the filament jumps upward and forms a current sheet according to the model by Forbes and Priest. When the current sheet becomes stretched, magnetic islands form and coalescence of islands occurs at locations of enhanced resistivity, initiating particle acceleration and plasma heating; *(c)* the lowest lying loops relax after reconnection and become filled due to chromospheric evaporation (loops with thick linestyle); *(d)* reconnection proceeds upward and involves higher lying, less sheared loops; *(e)* the arcade gradually fills up with filled loops; *(f)* the last reconnecting loops have no shear and are oriented perpendicular to the neutral line. At some point the filament disconnects completely from the flare arcade and escapes into interplanetary space.

in the much hotter tenuous coronal plasma. On the solar disk, these cool dense features appear dark in Hα or EUV images, in absorption against the bright background, and are called *filaments*, while the same structures appear bright above the limb, in emission against the dark sky background, where they are called *prominences*. Thus, *filaments* and *prominences* are identical structures physically, while their dual name just reflects a different observed location (inside or outside the disk). A further distinction is made regarding their dynamic nature: *quiescent filaments/prominences* are long-lived stable structures that can last for several months, while *eruptive filaments/prominences* are usually associated with flares and CMEs (see example in Fig. 16).

6.3 Solar Flare Models

A flare process is associated with a rapid energy release in the solar corona, believed to be driven by stored nonpotential magnetic energy and triggered by an instability in the magnetic configuration. Such an energy release process results in acceleration of nonthermal particles and in heating of coronal/chromospheric plasma. These processes emit radiation in almost all wavelengths: radio, white light, EUV, soft X-rays, hard X-rays, and even gamma-rays during large flares. The energy range

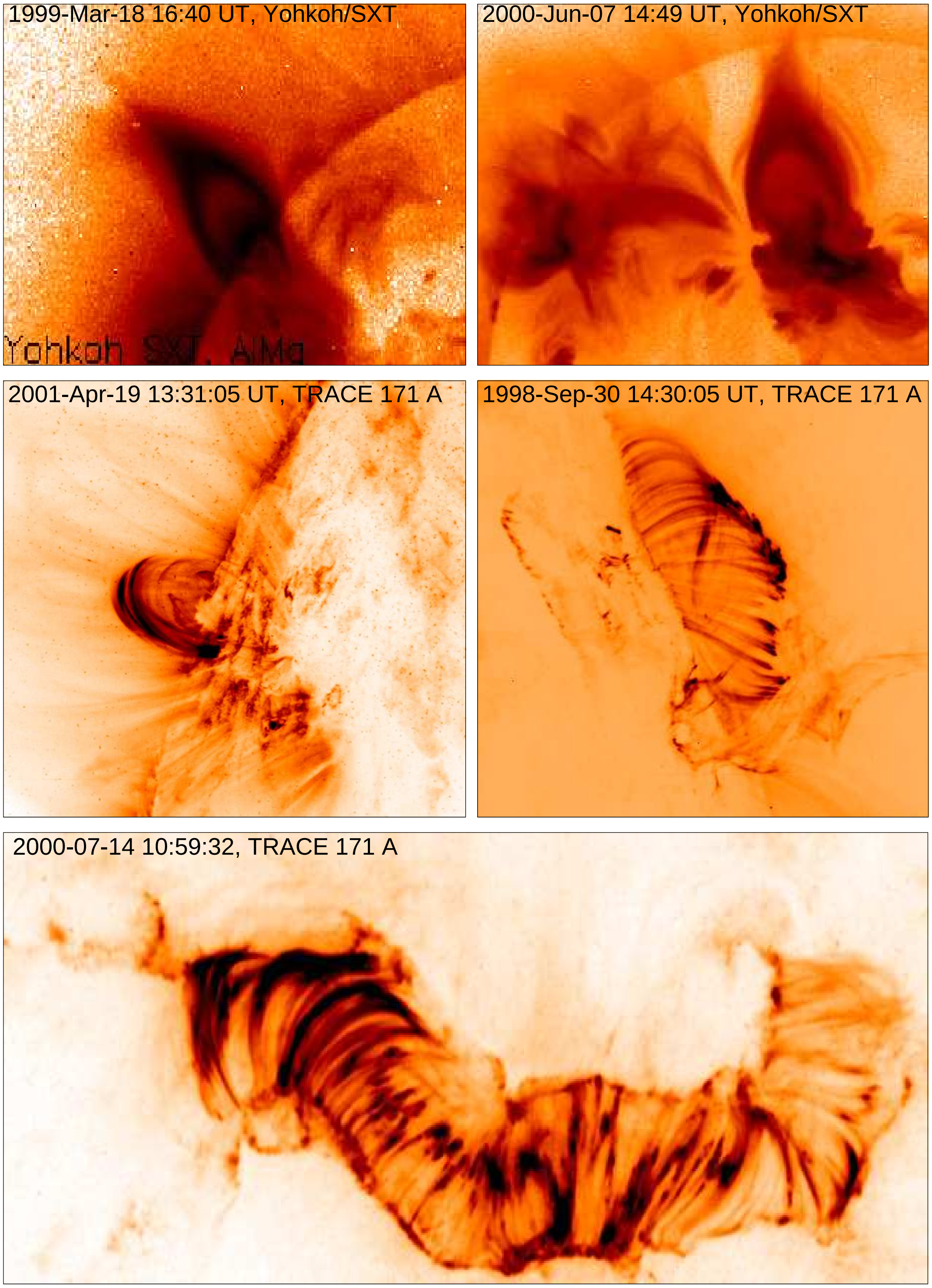

Figure 18: Soft X-ray and EUV images of flare loops and flare arcades with bipolar structure. Yohkoh/SXT observed flares (1999-Mar-18, 16:40 UT, and 2000-Jun-07, 14:49 UT) with “candle-flame”-like cusp geometry during ongoing reconnection, while TRACE sees postflare loops once they cooled down to $1-2$ MK, when they already relaxed into a near-dipolar state. Examples are shown for a small flare (the 2001-Apr-19 flare, 13:31 UT, GOES class M2), and for two large flares with long arcades, seen at the limb (1998-Sep-30, 14:30 UT) and on the disk (the 2000-Jul-14, 10:59 UT, X5.7 flare), (courtesy of Yohkoh/ISAS and TRACE/NASA).

of flares extends over many orders of magnitude. Small flares that have an energy content of 10^{-6} to 10^{-9} of the largest flares fall into the categories of microflares and nanoflares (Fig. 14), which are observed not only in active regions, but also in quiet Sun regions. Some of the microflares and nanoflares have been localized above the photospheric network, and are thus also dubbed *network flares* or *network heating events*. There is also a number of small-scale phenomena with rapid time variability for which it is not clear whether they represent miniature flare processes, such as *active region transients*, *explosive events*, *blinkers*, etc. It is conceivable that some are related to *photospheric* or *chromospheric* magnetic reconnection processes, in contrast to flares that always involve *coronal* magnetic reconnection processes.

The best known flare/CME models entail magnetic reconnection processes that are driven by a rising filament/prominence, by flux emergence, by converging flows, or by shear motion along the neutral line. Flare scenarios with a driver perpendicular to the neutral line (rising prominence, flux emergence, convergence flows) are formulated as 2D reconnection models, while scenarios that involve shear along the neutral line (tearing-mode instability, quadrupolar flux transfer, the magnetic breakout model, sheared arcade interactions) require 3D descriptions. A 2D reconnection model involving a *magnetic X-point* is shown in Fig. 17 (left), while a generalized 3D version involving a highly-sheared neutral line is sketched in Fig. 17 (right). There are more complex versions like the *magnetic breakout model*, where a second arcade triggers reconnection above a primary arcade. Observational evidence for magnetic reconnection in flares includes the 3D geometry, reconnection inflows, outflows, detection of shocks, jets, ejected plasmoids, and secondary effects like particle acceleration, conduction fronts, and chromospheric evaporation processes. Flare images in soft X-rays often show the cusp-shaped geometry of reconnecting field lines (Fig. 18, top), while EUV images invariably display the relaxed post-reconnection field lines after the flare loops cooled down to EUV temperatures in the postflare phase (Fig. 18, middle and bottom).

6.4 Flare Plasma Dynamics

The flare plasma dynamics and associated thermal evolution during a flare consists of a number of sequential processes: plasma heating in coronal reconnection sites, chromospheric flare plasma heating (either by precipitating nonthermal particles and/or downward propagating heat conduction fronts), chromospheric evaporation in the form of upflowing heated plasma, and cooling of postflare loops. The initial heating of the coronal plasma requires anomalous resistivity, because Joule heating with classical resistivity is unable to explain the observed densities, temperatures, and rapid time scales in flare plasmas. Other forms of coronal flare plasma heating, such as slow shocks, electron beams, proton beams, or inductive currents are difficult to constrain with currently available observables. The second stage of chromospheric heating is more thoroughly explored, based on the theory of the thick-target model, with numeric hydrodynamic simulations, and with particle-in-cell simulations. Important diagnostics on chromospheric heating are also available from Hα, white light, and UV emission, but quantitative modeling is still quite difficult because of the chromospheric opacities and partial ionization. The third stage of chromospheric evaporation has been extensively explored with hydrodynamic simulations, in particular to explain the observed Doppler shifts in soft X-ray lines, while application of spatial models to imaging data is quite sparse. Also certain types of slow-drifting radio bursts seem to contain information on the motion of chromospheric evaporation fronts. The fourth stage of postflare loop cooling is now understood to be dominated by thermal conduction initially, and by radiative cooling later on. However, spatio-temporal temperature modeling of flare plasmas (Fig. 19) has not yet been fitted to observations in detail.

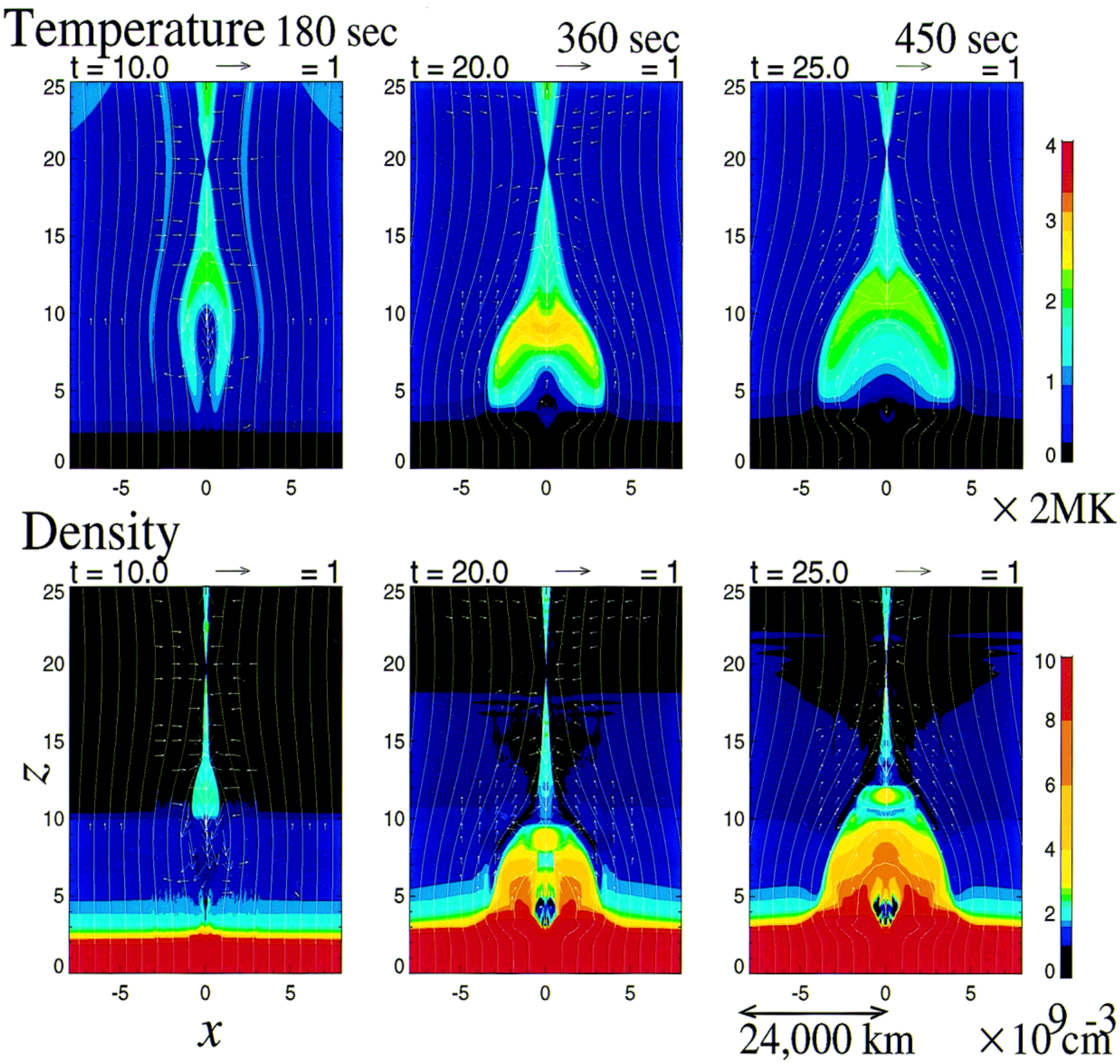

Figure 19: 2D numerical MHD simulation of a solar flare with chromospheric evaporation and anisotropic heat conduction in the framework of a 2D magnetic reconnecting geometry. The temporal evolution of the plasma temperature (top row) and density (bottom row) is shown. The temperature and density scale is shown in the bars on the right side. The simulation illustrates the propagation of thermal conduction fronts and the upflows of chromospheric plasma in response (courtesy of Takaaki Yokoyama and Kazunari Shibata).

6.5 Particle Acceleration and Kinematics

Particle acceleration in solar flares is mostly explored by theoretical models, because neither macroscopic nor microscopic electric fields are directly measurable by remote-sensing methods. The motion of particles can be described in terms of acceleration by parallel electric fields, drift velocities caused by perpendicular forces (i.e., $E \times B$-drifts), and gyromotion caused by the Lorentz force of the magnetic field. Theoretical models of particle acceleration in solar flares can be broken down into three groups: (1) DC electric field acceleration, (2) stochastic or second-order Fermi acceleration, and (3) shock acceleration. In the models of the first group, there is a paradigm shift from large-scale DC

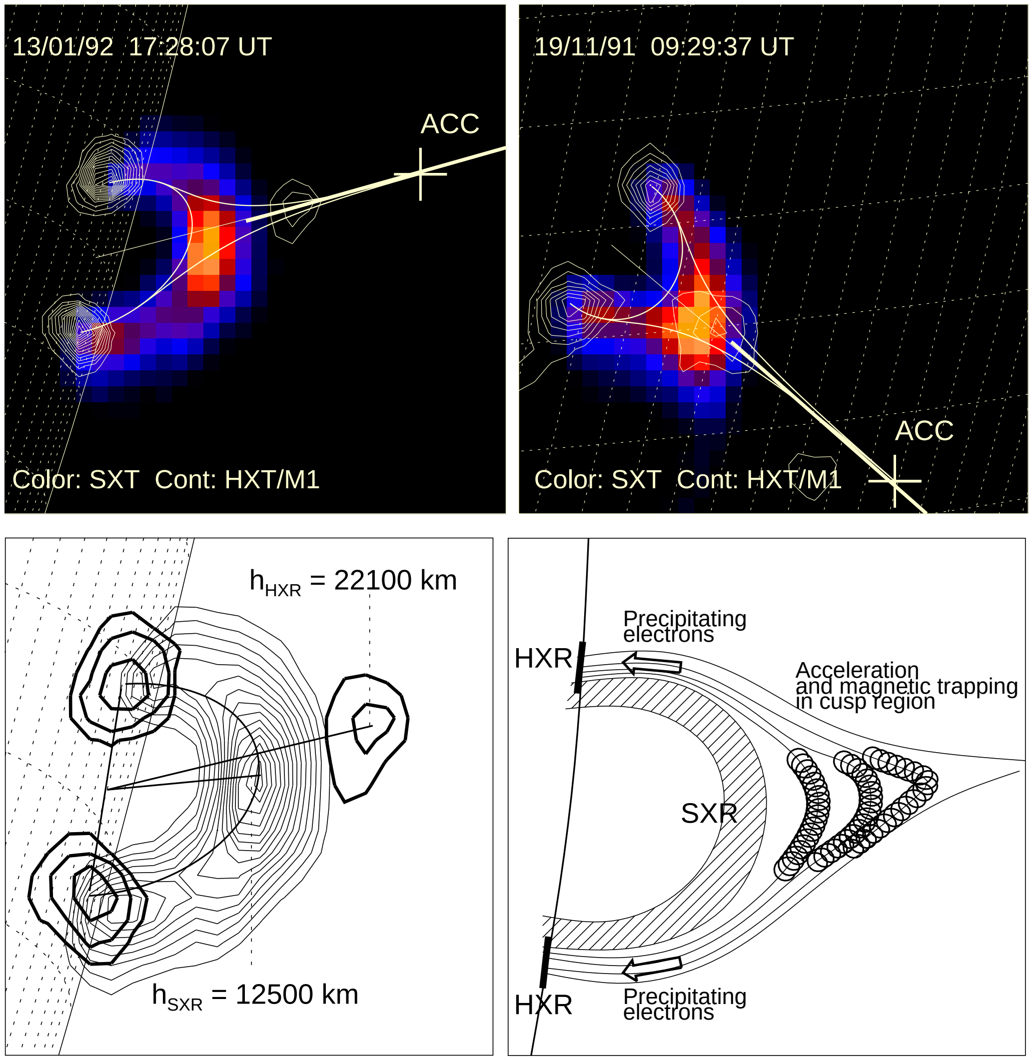

Figure 20: *Top:* The geometry of the acceleration region inferred from direct detections of above-the-looptop hard X-ray sources with Yohkoh/HXT (contours) and simultaneous modeling of electron time-of-flight distances based on energy-dependent time delays of $20-200$ keV hard X-ray emission measured with BATSE/CGRO (crosses marked with ACC). Soft X-rays detected with Yohkoh/SXT or thermal hard X-ray emission from the low-energy channel of Yohkoh/HXT/Lo are shown in colors, outlining the flare loops. *Bottom:* The observations in the left panel show a Yohkoh/HXT $23-33$ keV image (thick contours) and Be119 *SXT* image (thin contours) of the Masuda flare, 1992-Jan-13, 17:28 UT. The interpretation of the above-the-looptop source is that temporary trapping occurs in the acceleration region in the cusp region below the reconnection point (bottom right).

electric fields (of the size of flare loops) to small-scale electric fields (of the size of magnetic islands produced by the tearing mode instability). The acceleration and trajectories of particles is studied more realistically in the inhomogeneous and time-varying electromagnetic fields around magnetic X-points and O-points of magnetic reconnection sites, rather than in static, homogeneous, large-scale Parker-type current sheets. The second group of models entails stochastic acceleration by gyroresonant wave-particle interactions, which can be driven by a variety of electrostatic and electromagnetic waves, supposed that wave turbulence is present at a sufficiently enhanced level and that the MHD turbulence cascading process is at work. The third group of acceleration models includes a rich variety of shock acceleration models, which is extensively explored in magnetospheric physics and could cross-fertilize solar flare models. Two major groups of models are studied in the context of solar flares (i.e., first-order Fermi acceleration or shock-drift acceleration, and diffusive shock acceleration). New aspects are that shock acceleration is now applied to the outflow regions of coronal magnetic reconnection sites, where first-order Fermi acceleration at the standing fast shock is a leading candidate. Traditionally, evidence for shock acceleration in solar flares came mainly from radio type II bursts. New trends in this area are the distinction of different acceleration sites that produce type II emission: flare blast waves, the leading edge of CMEs (bowshock), and shocks in internal and lateral parts of CMEs. In summary we can say that (1) all three basic acceleration mechanisms seem to play a role to a variable degree in some parts of solar flares and CMEs, (2) the distinction between the three basic models become more blurred in more realistic (stochastic) models, and (3) the relative importance and efficiency of various acceleration models can only be assessed by including a realistic description of the electromagnetic fields, kinetic particle distributions, and MHD evolution of magnetic reconnection regions pertinent to solar flares.

Particle kinematics, the quantitative analysis of particle trajectories, has been systematically explored in solar flares by performing high-precision energy-dependent time delay measurements with the large-area detectors of the *Compton Gamma-Ray Observatory (CGRO)*. There are essentially five different kinematic processes that play a role in the timing of nonthermal particles energized during flares: (1) acceleration, (2) injection, (3) free-streaming propagation, (4) magnetic trapping, and (5) precipitation and energy loss. The time structures of hard X-ray and radio emission from nonthermal particles indicate that the observed energy-dependent timing is dominated either by free-streaming propagation (obeying the expected electron time-of-flight dispersion) or by magnetic trapping in the weak-diffusion limit (where the trapping times are controlled by collisional pitch angle scattering). The measurements of the velocity dispersion from energy-dependent hard X-ray delays allows then to localize the acceleration region, which was invariably found in the cusp of postflare loops (Fig. 20).

6.6 Hard X-Ray Emission

Hard X-ray emission is produced by energized electrons via collisional bremsstrahlung, most prominently in the form of thick-target bremsstrahlung when precipitating electrons hit the chromosphere. Thin-target bremsstrahlung may be observable in the corona for footpoint-occulted flares. Thermal bremsstrahlung dominates only at energies of $\lesssim 15$ keV. Hard X-ray spectra can generally be fitted with a thermal spectrum at low energies and with a single- or double-powerlaw nonthermal spectrum at higher energies. Virtually all flares exhibit fast (subsecond) pulses in hard X-rays, which scale proportionally with flare loop size and are most likely spatio-temporal signatures of bursty magnetic reconnection events. The energy-dependent timing of these fast subsecond pulses exhibit electron time-of-flight delays from the propagation between the coronal acceleration site and the chromospheric thick-target site. The inferred acceleration site is located about 50% higher than the soft X-ray flare loop height, most likely near X-points of magnetic reconnection sites (Fig. 20). The more gradually varying hard X-ray emission exhibits an energy-dependent time delay with opposite sign, which corresponds to the timing of the collisional deflection of trapped electrons. In many flares, the time evolution of soft X-rays roughly follows the integral of the hard X-ray flux profile, which is called the *Neupert effect*. Spatial structures of hard X-ray sources include: (1) footpoint sources produced by thick-target bremsstrahlung; (2) thermal hard X-rays from flare looptops; (3) "above-the-looptop" (Masuda-type) sources that result from nonthermal bremsstrahlung from electrons that are either trapped in the acceleration region or interact with reconnection shocks; (4) hard X-ray sources associated with upward soft X-ray ejecta; and (5) hard X-ray halo or albedo sources due to backscattering at the photosphere. In spatially extended flares, the footpoint sources assume ribbon-like morphology if mapped with sufficient sensitivity. The monthly hard X-ray flare rate varies about a

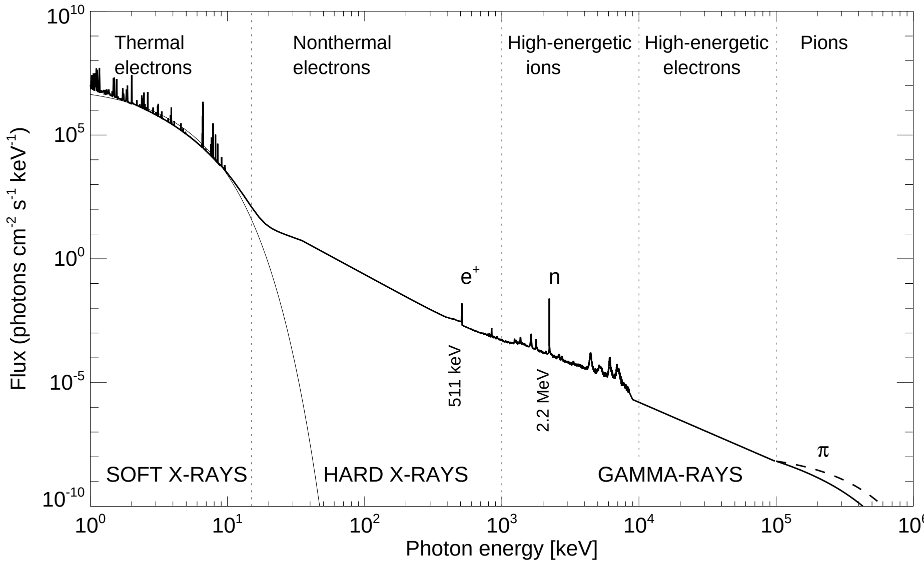

Figure 21: Composite photon spectrum of a large flare, extending from soft X-rays (1−10 keV), hard X-rays (10 keV−1 MeV), to gamma-rays (1 MeV−100 GeV). The energy spectrum is dominated by different processes: by thermal electrons (in soft X-rays), bremsstrahlung from nonthermal electrons (in hard X-rays), nuclear de-excitation lines (in $\approx 0.5 - 8$ MeV gamma-rays), by bremsstrahlung from high-energetic electrons (in $\approx 10 - 100$ MeV gamma-rays), and by pion-decay (in $\gtrsim 100$ MeV gamma-rays). Note also the prominent electron-positron annihilation line (at 511 keV) and the neutron capture line (at 2.2 MeV).

factor of 20 during the solar cycle, similar to magnetic flux variations implied by the monthly sunspot number, as expected from the magnetic origin of flare energies.

6.7 Gamma-Ray Emission

The energy spectrum of flares (Fig. 21) in gamma-ray wavelengths (0.5 MeV$-$1 GeV) is more structured than in hard X-ray wavelengths ($20 - 500$ keV), because it exhibits both continuum emission as well as line emission. There are at least six different physical processes that contribute to gamma-ray emission: (1) electron bremsstrahlung continuum emission; (2) nuclear de-excitation line emission; (3) neutron capture line emission at 2.223 MeV; (4) positron annihilation line emission at 511 keV; (5) pion-decay radiation at $\gtrsim 50$ MeV; and (6) neutron production. The ratio of continuum to line emission varies from flare to flare and gamma-ray lines can completely be overwhelmed in electron-rich flares or flare phases. When gamma-ray lines are present, they provide a diagnostic of the elemental abundances, densities, and temperatures of the ambient plasma in the chromosphere, as well as of the directivity and pitch angle distribution of the precipitating protons and ions that have been accelerated in coronal flare sites, presumably in magnetic reconnection regions. Critical issues that have been addressed in studies of gamma-ray data are the maximum energies of coronal acceleration mechanisms, the ion/electron ratios (because selective acceleration of ions indicate gyroresonant interactions), the ion/electron timing (to distinguish between simultaneous or second-step acceleration), differences in ion/electron transport (e.g., neutron sources were recently found to be displaced from electron sources), and the first ionization potential (FIP) effect of chromospheric abundances (indicating enhanced abundances of certain ions that could be preferentially accelerated by gyroresonant interactions). Although detailed modeling of gamma-ray line profiles provides significant constraints on elemental abundances and physical properties of the ambient chromospheric plasma, as well as on the energy and pitch angle distribution of accelerated particles, little information or constraints could be retrieved about the time scales and geometry of the acceleration mechanisms, using gamma-

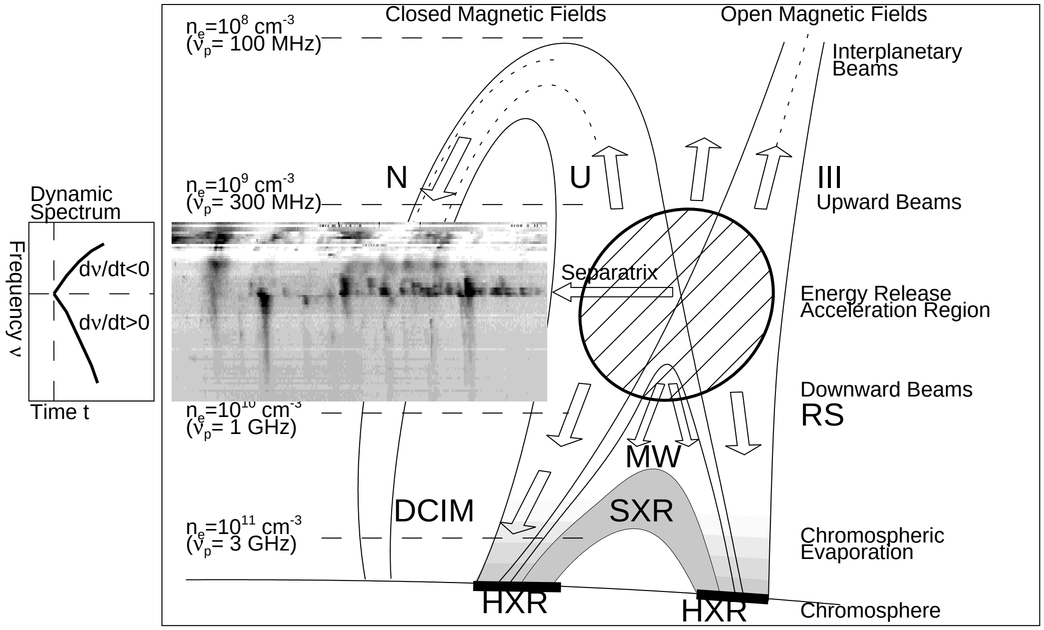

Figure 22: Radio burst types in the framework of the standard flare scenario: The acceleration region is located in the reconnection region above the soft X-ray-bright flare loop, accelerating electron beams in the upward direction (type III, U, N bursts) and in the downward direction (type RS, DCIM bursts). Downward moving electron beams precipitate to the chromosphere (producing hard X-ray emission and driving chromospheric evaporation), or remain transiently trapped, producing microwave (MW) emission. Soft X-ray loops become subsequently filled up, with increasing footpoint separation as the X-point rises. The insert shows a dynamic radio spectrum (*ETH* Zurich) of the 92-Sept-06, 1154 UT, flare, showing a separatrix between type III and type RS bursts at ≈ 600 MHz, probably associated with the acceleration region.

ray data. Nevertheless, the high spectral and imaging resolution of the recently launched RHESSI spacecraft faciliates promising new data for a deeper understanding of ion acceleration in solar flares.

6.8 Radio Emission

Radio emission in the solar corona is produced by thermal, nonthermal, up to high-relativistic electrons, and thus provides a lot of useful diagnostics complementary to EUV, soft X-rays, hard X-rays, and gamma-rays. Thermal or Maxwellian distribution functions produce in radio wavelengths either free-free emission (bremsstrahlung) for low magnetic field strengths and gyroresonance emission in locations of high magnetic field strengths, such as above sunspots, which are both called incoherent emission mechanisms. Since EUV and soft X-ray emission occurs in the optically thin regime, the emissivity adds up linearly along the line-of-sight. Free-free emission in radio is somewhat more complicated, because the optical thickness depends on the frequency, which allows direct measurement of the electron temperature in optically thick coronal layers in metric and decimetric frequencies up to $\nu \lesssim 1$ GHz. Above ≈ 2 GHz, free-free emission becomes optically thin in the corona, but gyroresonance emission at harmonics of $s \approx 2, 3, 4$ dominates in strong-field regions. In flares, high-relativistic electrons are produced that emit gyrosynchrotron emission, which allows for detailed modeling of precipitating and trapped electron populations in time profiles recorded at different microwave frequencies.

Unstable non-Maxwellian particle velocity distributions, which have a positive gradient in parallel (beams) or perpendicular (losscones) direction to the magnetic field, drive gyroresonant wave-particle interactions that produce coherent wave growth, detectable in the form of coherent radio emission. Two natural processes that provide these conditions are dispersive electron propagation (producing beams) and magnetic trapping (producing losscones). The wave-particle interactions produce growth of Langmuir waves, upper-hybrid waves, and electron-cyclotron maser emission, leading to a variety of radio burst types (type I, II, III, IV, V, DCIM; Fig. 22), which have been mainly explored from (non-imaging) dynamic spectra, while imaging observations have been rarely obtained. Although there is much theoretical understanding of the underlying wave-particle interactions, spatio-temporal modeling of imaging observations is still in its infancy. A solar-dedicated, frequency-agile imager with many frequencies (FASR) is in planning stage and might provide more comprehensive observations.

6.9 Coronal Mass Ejections

Every star is losing mass, caused by dynamic phenomena in its atmosphere, which accelerate plasma or particles beyond the escape speed. Inspecting the Sun, our nearest star, we observe two forms of mass loss: the steady *solar wind outflow* and the sporadic ejection of large plasma structures, termed *coronal mass ejections (CMEs)*. The solar wind outflow amounts to $\approx 2 \times 10^{-10}$ (g cm^{-2} s^{-1}) in coronal holes, and to $\lesssim 4 \times 10^{-11}$ (g cm^{-2} s^{-1}) in active regions. The phenomenon of a CME occurs with a frequency of about 1 event per day, carrying a mass in the range of $m_{CME} \approx 10^{14} - 10^{16}$ g, which corresponds to an average mass loss rate of $m_{CME}/(\Delta t \cdot 4\pi R_\odot^2) \approx 2 \times 10^{-14} - 2 \times 10^{-12}$ (g cm^{-2} s^{-1}), which is $\lesssim 1\%$ of the solar wind mass loss in coronal holes, or $\lesssim 10\%$ of the solar wind mass in active regions. The transverse size of CMEs can cover a fraction up to more than a solar radius, and the ejection speed is in the range of $v_{CME} \approx 10^2 - 10^3$ (km s^{-1}). A CME structure can have the geometric shape of a fluxrope, a semi-shell, or a bubble (like a light bulb, see Fig. 24), which is the subject of much debate, because of ambiguities from line-of-sight projection effects and the optical thinness. There is a general consensus that a CME is associated with a release of magnetic energy in the solar corona, but its relation to the flare phenomenon is controversial. Even big flares (at least GOES M-class) have no associated CMEs in 40% of the cases. A long-standing debate focused on the question of whether a CME is a by-product of the flare process or vice versa. This question has been settled in the view that flares and CMEs are two aspects of a large-scale magnetic energy release, but the two terms evolved historically from two different observational manifestations (i.e., *flares* denoting mainly the emission in hard X-rays, soft X-rays, and radio, while *CMEs* being referred to the white-light emission of the erupting mass in the outer corona and heliosphere). Recent studies, however, clearly established the co-evolution of both processes triggered by a common magnetic instability. A CME is a dynamically evolving plasma structure, propagating outward from the Sun into interplanetary space, carrying a frozen-in magnetic flux and expanding in size. If a CME structure travels towards the Earth, which is mostly the case when launched in the western solar hemisphere, due to the curvature of the *Parker spiral* interplanetary magnetic field, such an *Earth-directed* event can engulf the Earth's magnetosphere and generate significant geomagnetic storms. Obviously such geomagnetic storms can cause disruptions of global communication and navigation networks, can cause failures of satellites and commercial power systems, and thus are subject of high interest.

Theoretical models include five categories: (1) thermal blast models, (2) dynamo models, (3) mass loading models, (4) tether release models, and (5) tether straining models. Numerical MHD simulations of CMEs are currently produced by combinations of a fine-scale grid that entails the corona and a connected large-scale grid that encompasses propagation into interplanetary space, which can reproduce CME speeds, densities, and the coarse geometry. The trigger that initiates the origin of a CME seems to be related to previous photospheric shear motion and subsequent kink instability of twisted structures (Fig. 23). The geometry of CMEs is quite complex, exhibiting a variety of topolog-

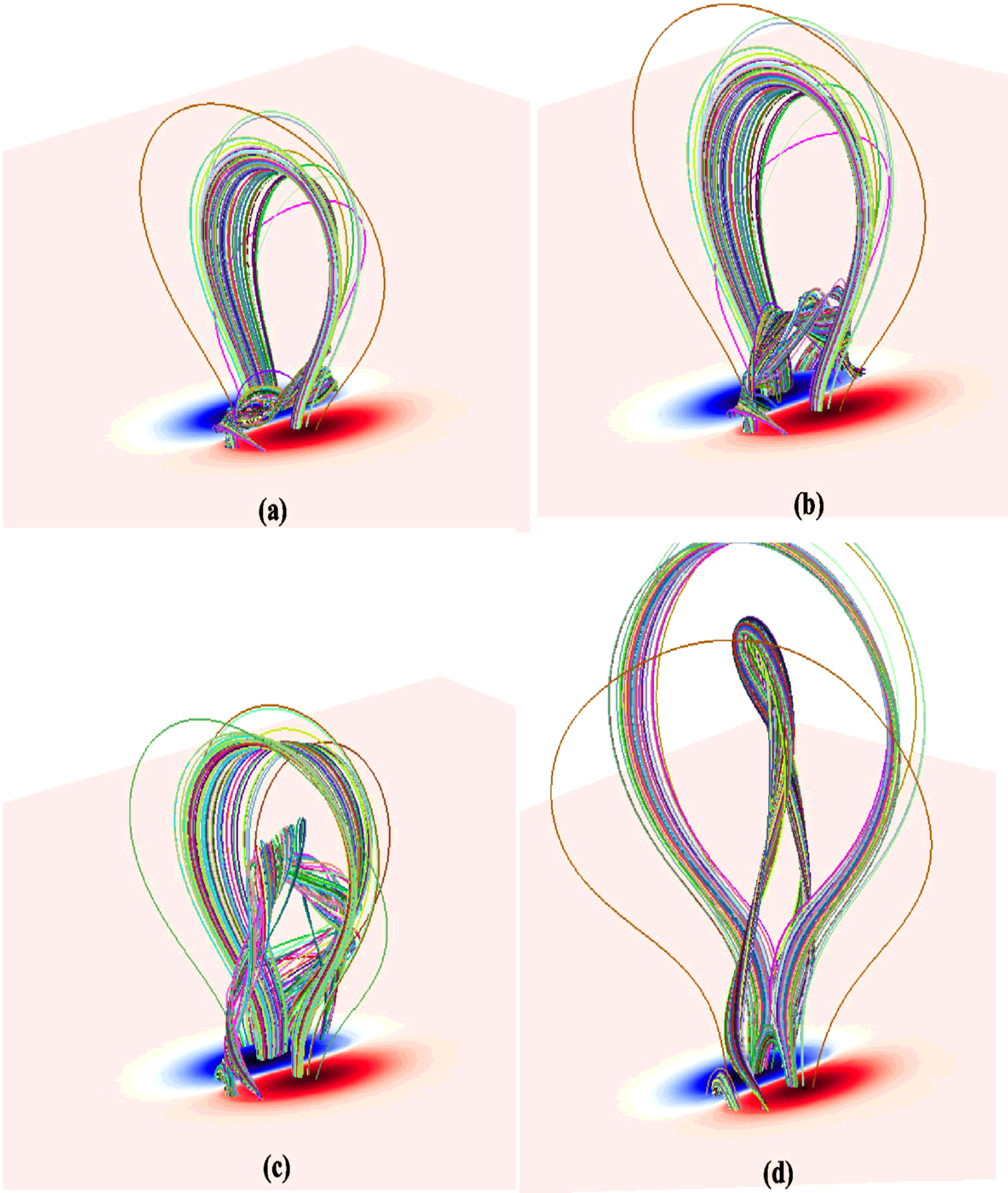

Figure 23: Numerical MHD simulation of the evolution of a CME, driven by turbulent diffusion. The four panels correspond to the times (a) t=850, (b) t=950, (c) t=1050, and (d) t=1150, where viscous relaxation is started at t=850, triggering a global disruption involving opening, reconnection through the overlying arcade and below, and the formation of a current sheet, associated with a high dissipation of magnetic energy and a strong increase of kinetic energy (courtesy of T. Amari).

ical shapes from spherical semi-shells to helical fluxropes (Fig. 24), and the density and temperature structure of CMEs is currently investigated with multi-wavelength imagers. The height-time, velocity, and acceleration profiles of CMEs seems to establish two different CME classes: gradual CMEs associated with propagating interplanetary shocks, and impulsive CMEs caused by coronal flares. The total energy of CMEs (i.e., the sum of magnetic, kinetic, and gravitational energy), seem to be con-

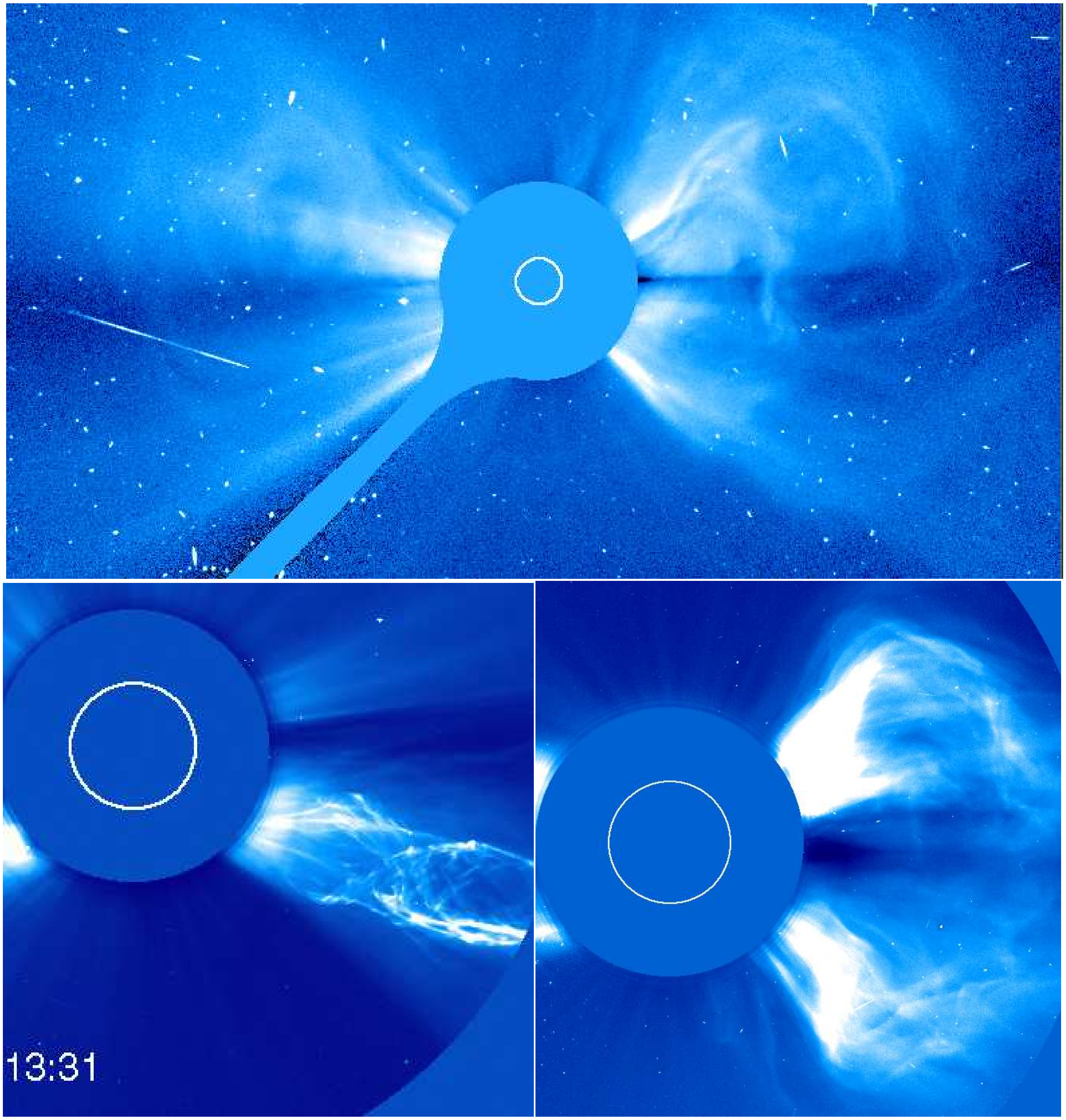

Figure 24: LASCO C3 image of a halo CME of 1998-May-6 (top), an erupting prominence of 1998-Jun-02, 13:31 UT (bottom left), and a large CME of 1997-Nov-06, 12:36 UT (bottom right), (courtesy of SoHO/LASCO and NASA).

served in some events, and the total energy of CMEs is comparable to the energy range estimated from flare signatures. A closely associated phenomenon to CMEs is *coronal dimming* (Fig. 13), which is interpreted in terms of an evacuation of coronal mass during the launch of a CME. The propagation of CMEs in interplanetary space provides diagnostic on the heliospheric magnetic field, the solar wind, interplanetary shocks, solar energetic particle (SEP) events, and interplanetary radio bursts.

7 Final Comments

The study of the Sun, our nearest Star, is systematically moving from morphological observations (sunspots, active regions, filaments, flares, CMEs) to a more physics-based modeling and theoretical understanding, in terms of nuclear physics, magneto-convection, magneto-hydrodynamics, magnetic reconnection, and particle physics processes. The major impact of physics-based modeling came from the multi-wavelength observations from solar-dedicated space-based (SMM, Yohkoh, CGRO, SoHO, TRACE, RHESSI) and ground-based instruments (in radio, Hα, and white-light wavelengths). Major achievements over the last decades are the advancement of new disciplines such as *helioseismology* and *coronal seismology*, the solution of the *neutrino problem*, while there are still unsolved outstanding problems such as the *coronal heating problem* and *particle acceleration mechanisms*. We can optimistically expect substantial progress from future solar-dedicated space missions (Solar-B, STEREO, Solar Dynamics Observatory (SDO), Solar Orbiter, Solar Probe) and ground-based instruments (SOLIS, ATST, FASR).

8 Bibliography

Aschwanden,M.J. 2004, *"Physics of the Solar Corona - An Introduction"*, Praxis Publishing Ltd.: Chichester UK, and Springer: New York.

Benz,A.O. 1993, (2003; 2^{nd} edition), *"Plasma Astrophysics, Kinetic Processes in Solar and Stellar Coronae"*, Kluwer Academic Publishers: Dordrecht, The Netherlands.

Cox,A.N. (ed.) 2000 (4^{th} edition), *"Allen's Astrophysical Quantities"*, American Institute of Physics (AIP) Press, Springer: New York.

Dwivedi,B.N. 2003, *The Dynamic Sun*, Cambridge University Press: Cambridge.

Foukal,P.V. 1990, (2003; 2^{nd} edition), *"Solar Astrophysics"*, John Wiley and Sons, Inc.: New York.

Golub,L. & Pasachoff,J.M. 2001, *"Nearest Star: The Surprising Science of Our Sun"*, Harvard University Press: Cambridge.

Golub,L. and Pasachoff,J.M. 1997, *"The Solar Corona"*, Cambridge University Press: Cambridge.

Lang,K.R. 2001, *"The Cambridge Encyclopedia of the Sun"*, Cambridge University Press: Cambridge.

Murdin,P. (ed.) 2000, *"Encyclopedia of Astronomy and Astrophysics"*, Institute of Physics Publishing, Grove's Dictionaries, Inc.: New York.

Schrijver,C.J. & Zwaan,C. 2000, *Solar and Stellar Magnetic Activity"*, Cambridge University Press: Cambridge.

Stix,M. 1989, (2002; 2^{nd} edition), *"The Sun"*, Springer: New York.

Zirker,J.B. 2002, *"Journey from the Center of the Sun"*, Princeton University Press: Princeton.